JCB Journal of Cell Biology

ARTICLE

The molecular recognition of phosphatidic acid by an amphipathic helix in Opi1

Harald F. Hofbauer[1,2,6], Michael Gecht[1,2,3], Sabine C. Fischer[1,4], Anja Seybert[1], Achilleas S. Frangakis[1], Ernst H.K. Stelzer[1,4], Roberto Covino[3], Gerhard Hummer[3,5], and Robert Ernst[6]

A key event in cellular physiology is the decision between membrane biogenesis and fat storage. Phosphatidic acid (PA) is an important intermediate at the branch point of these pathways and is continuously monitored by the transcriptional repressor Opi1 to orchestrate lipid metabolism. In this study, we report on the mechanism of membrane recognition by Opi1 and identify an amphipathic helix (AH) for selective binding of PA over phosphatidylserine (PS). The insertion of the AH into the membrane core renders Opi1 sensitive to the lipid acyl chain composition and provides a means to adjust membrane biogenesis. By rational design of the AH, we tune the membrane-binding properties of Opi1 and control its responsiveness in vivo. Using extensive molecular dynamics simulations, we identify two PA-selective three-finger grips that tightly bind the PA phosphate headgroup while interacting less intimately with PS. This work establishes lipid headgroup selectivity as a new feature in the family of AH-containing membrane property sensors.

Introduction

Lipids are actively involved in cellular signaling and serve as major determinants of the organellar identity (Bigay and Antonny, 2012; Holthuis and Menon, 2014). Numerous molecular processes occur at the surfaces of organelles, and the selective membrane recruitment of cytosolic effectors is crucial to control lipid metabolism, vesicular transport, and cellular signaling (Odorizzi et al., 2000; Antonny, 2011; Jacquemyn et al., 2017). The organelles of eukaryotic cells are composed of hundreds of lipid species (Zinser et al., 1991; Ejsing et al., 2009; Klemm et al., 2009; Gerl et al., 2012). Despite a continuous exchange of membrane material, organelles maintain their characteristic lipid compositions and surface properties (Bigay and Antonny, 2012; de Kroon et al., 2013; Antonny et al., 2015; Ernst et al., 2018). A particularly powerful mechanism of membrane homeostasis is a feedback control by membrane-associated transcription regulators and programs that can either sense the level of individual lipids such as cholesterol (Goldstein et al., 2006) or phosphoinositides (Laplante and Sabatini, 2012) or respond to bulk physicochemical membrane properties (Ernst et al., 2018; Radanović et al., 2018).

The decision to direct lipid precursors to either membrane biogenesis or fat storage represents a key regulatory step in cellular physiology, and the transcriptional programs underlying these processes must be carefully controlled (Henry et al., 2012; Puth et al., 2015). Phosphatidic acid (PA) is a class of glycerophospholipids at the branch point of membrane lipid biosynthesis and triacylglycerol production (Athenstaedt and Daum, 1999; Ernst et al., 2016). PA lipids act as second messengers, and their signaling function is conserved in yeast (Loewen et al., 2004), plants (Testerink and Munnik, 2011), and mammals (Wang et al., 2006; Laplante and Sabatini, 2012). A misregulated metabolism of PA has been implicated in cancer biology (Foster, 2009; Laplante and Sabatini, 2012), but the molecular mechanisms of PA recognition remain elusive (Liu et al., 2013).

Given the central position of PA lipids in cellular physiology and the lipid metabolic network (Henry et al., 2012), it is not surprising that cells established mechanisms to monitor the level of PA. Opi1 is a soluble transcriptional repressor in *Saccharomyces cerevisiae* controlling the expression of lipid biosynthetic genes containing an upstream activating sequence responsive to inositol (UAS_{INO}). These genes are involved in the production of the major glycerophospholipid classes phosphatidylcholine (PC), phosphatidylethanolamine (PE), phosphatidylinositol (PI), and phosphatidylserine (PS), for which PA lipids serve as precursors (Henry et al., 2012). When the level of PA is high, Opi1 binds to PA at the ER membrane and is prevented from entering the nucleus, thereby allowing for the expression of UAS_{INO}

[1]Buchmann Institute for Molecular Life Sciences, Goethe University Frankfurt, Frankfurt, Germany; [2]Institute of Biochemistry, Biocenter, Goethe University Frankfurt, Frankfurt, Germany; [3]Department of Theoretical Biophysics, Max Planck Institute of Biophysics, Frankfurt, Germany; [4]Physical Biology, Interdisciplinary Center for Neuroscience, Goethe University Frankfurt, Frankfurt, Germany; [5]Institute for Biophysics, Goethe University Frankfurt, Frankfurt, Germany; [6]Institute of Medical Biochemistry and Molecular Biology, School of Medicine, University of Saarland, Homburg, Germany.

Correspondence to Robert Ernst: robert.ernst@uks.eu; Harald F. Hofbauer: harald.f.hofbauer@gmail.com.

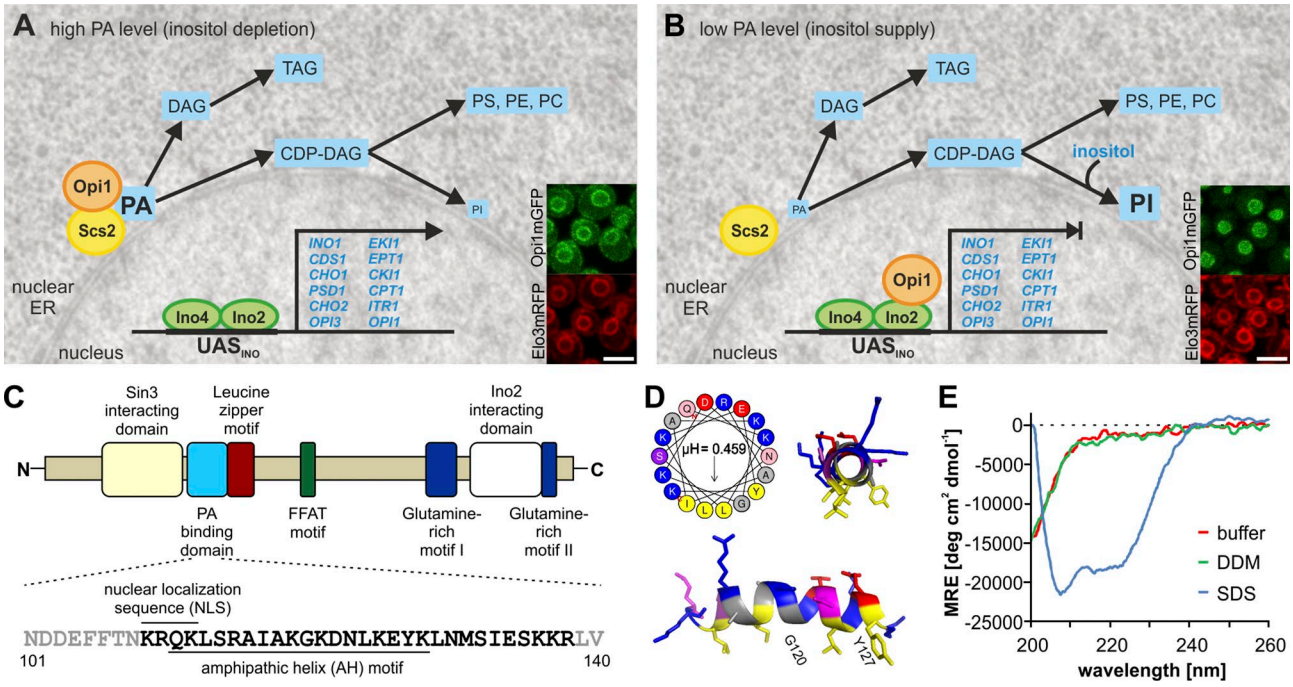

Figure 1. **Opi1 uses an AH to control glycerophospholipid metabolism. (A and B)** PA serves as a precursor for diacylglycerol (DAG) and triacylglycerol (TAG). Via cytidine diphosphate (CDP)-DAG, PA can also be converted in various other glycerophospholipids. When the level of PA is high, Opi1 binds to the ER membrane, thereby facilitating membrane biogenesis (A). When the PA level is low, Opi1 localizes to the nucleus and represses its target genes (B). Scs2 acts a coreceptor for Opi1. Inlets show micrographs Opi1-mGFP–expressing cells with Elo3-mRFP as ER marker. Bars, 5 µm. **(C)** Domain organization of Opi1 (404 aa) with the PA-interacting motif (aa 109–138; light blue), the leucine zipper motif (aa 139–160; brown), and the FFAT motif (aa 193–204; green) for Scs2 binding is schematically indicated. The nuclear localization sequence (aa 109–112) and the PA-binding domain are highlighted (aa 111–128). **(D)** Visualization of the putative AH ($Opi1^{111–128}$) using HeliQuest and PyMOL. **(E)** CD spectroscopic analysis of the $Opi1^{111–128}$ synthetic peptide in a sodium phosphate buffer in the absence of detergent (buffer) or in the presence of either 20 mM DDM or 20 mM SDS. MRE, mean residue ellipticity.

target genes (Fig. 1 A; Loewen et al., 2004). When PA is consumed, Opi1 is released from the ER, translocates into the nucleus, and represses membrane biogenesis genes (Fig. 1 B; Loewen et al., 2004). The direct binding of Opi1 to PA-rich membranes is assisted by the tail-anchored VAP orthologue protein Scs2 that binds the Opi1 FFAT domain (two phenylalanines in an acidic tract; aa 193–204) and acts as a coreceptor in the ER membrane (Fig. 1, A and C; Loewen et al., 2003, 2004). Inositol is a master regulator of this pathway (Jesch et al., 2005): When inositol is present in the medium, PA lipids are converted to PI, and Opi1 represses its target genes, including *INO1*, which encodes the rate-limiting enzyme for inositol biosynthesis (Fig. 1 B; Graves and Henry, 2000). Loss of Scs2, the coreceptor for Opi1, causes a constitutive repression of *INO1* and thus inositol auxotrophy, especially at elevated temperature (Loewen et al., 2004; Gaspar et al., 2017). Loss of Opi1, on the contrary, results in the derepression of lipid biosynthetic genes as indicated by the overproduction and secretion of inositol from cells, the so-called Opi^- phenotype (Greenberg et al., 1982).

Recent studies have suggested that the ER membrane recruitment of Opi1 is not only controlled by the level of anionic PA lipids but also by the lipid acyl chain composition (Hofbauer et al., 2014; Putta et al., 2016; Kassas et al., 2017). These observations provided a new perspective on the regulation of membrane biogenesis, with Opi1 mediating a crosstalk between fatty acid metabolism and glycerophospholipid biosynthesis. In fact, it was postulated that the PA-binding domain of Opi1 might form an amphipathic helix (AH; Ganesan et al., 2016) to engage in interactions both with the lipid headgroups of PA and with the hydrophobic core of the membrane. Although the preference of the Opi1 PA-binding domain for PA-containing and loosely packed membranes provided supporting evidence (Putta et al., 2016; Kassas et al., 2017), this possibility was not directly tested.

Given the simplicity of the negatively charged phosphate headgroup of PA, a particularly puzzling question remains: how do proteins distinguish between PA and other anionic lipids such as PS to confer specificity? In contrast to PS, PA can be deprotonated twice, yielding ionization states of either −1 or −2 (Kooijman et al., 2005). The pKa for the second deprotonation of PA is close to the physiological pH and greatly affected by the membrane context (Kooijman et al., 2005). The phosphate moiety of PS can be deprotonated only once, yielding an ionization state of −1 at physiological pH. Based on these findings, it was proposed that the intracellular pH provides an additional cue for the Opi1 regulatory system (Young et al., 2010). Despite these intriguing findings, it is still unclear whether specific structural features could endow a protein with PA selectivity. For example, the membrane-binding region of Spo20 ($Spo20^{62–79}$) has been established and optimized as PA-selective biosensor (Nakanishi et al., 2004; Kassas et al., 2012; Zhang et al., 2014), whereas $Spo20^{51–91}$ was later shown not to distinguish between anionic lipids such as PA, PS, and phosphoinositides when taking into account and compensating for different net charges of the headgroup (Horchani et al., 2014).

In this study, we present our efforts to better understand the molecular underpinnings of PA recognition by the Opi1 regulatory system. We validate the presence of an AH in the basic PA-binding region of Opi1 and establish the tuning of interfacial hydrophobicity as a powerful tool to manipulate membrane binding in vitro and membrane-dependent signaling in vivo. Using extensive atomistic molecular dynamics (MD) simulations, we identify two PA-selective three-finger grips, each formed by three basic residues on one side of the AH as a robust mechanism for selective PA binding. Intriguingly, lysine and arginine residues have nonequivalent functions in establishing PA selectivity, thereby excluding that PA recognition is solely dictated by electrostatics. This work establishes lipid headgroup selectivity of AHs as crucial contributors to the regulation of membrane biogenesis in yeast and to membrane recognition processes in general.

Results

To characterize the details of membrane recognition by Opi1, we focused on the PA-binding domain (Opi1$^{111–128}$; Loewen et al., 2004) adjacent to the nuclear localization sequence (KRQK; Opi1$^{109–112}$; Fig. 1 C). HeliQuest analysis (Gautier et al., 2008) of this region revealed a putative AH with a small hydrophobic and a large hydrophilic face and several basic amino acid residues, which are crucial for PA binding (Loewen et al., 2004; Fig. 1 D). The arrangement of hydrophobic and basic residues in the predicted AH of Opi1 resembles the AH of the membrane-sensor motif of Spo20 (Nakanishi et al., 2004) but differs from the serine-rich N-terminal AH of the PA-converting phosphatidate phosphatase Pah1 (Fig. S1, A–C; Karanasios et al., 2010). Using circular dichroism (CD) spectroscopy, we characterized the secondary structure of a synthetic peptide corresponding to the predicted AH (Opi1$^{111–128}$). The peptide was unstructured in aqueous buffer even in the presence of a hydrophobic matrix provided by dodecyl maltoside (DDM) micelles (Fig. 1 E). Only in the presence of SDS did the peptide adopt a helical secondary structure. These observations suggest that the PA-interacting motif of Opi1 has only a weak propensity to form an AH, if at all.

We hypothesized that the AH of Opi1 might form only upon membrane binding, similar to membrane-active antimicrobial peptides (Ladokhin and White, 1999; Shai, 1999) and amphipathic lipid packing sensor (ALPS) motifs (Drin and Antonny, 2010; Antonny, 2011). Because PA supports membrane binding of Opi1 (Loewen et al., 2004), we studied the secondary structure of the synthetic Opi1$^{111–128}$ peptide in the presence of liposomes with a PC-based matrix and with increasing molar fractions of PA (Fig. 2 A). The lipid mixtures were prepared from stocks of 1,2-dioleoyl-*sn*-glycero-3-phosphocholine (DOPC), 1-palmitoyl-2-oleoyl-*sn*-glycero-3-phosphocholine (POPC), and 1-palmitoyl-2-oleoyl-*sn*-glycero-3-phosphate (POPA) to generate liposomes differing in the lipid headgroup composition but not in the lipid acyl chain composition. The liposomes were composed of lipids with 75% monounsaturated and 25% saturated lipid acyl chains to match the molecular packing density of the ER (Kaiser et al., 2011; Covino et al., 2016). Liposome diameters of 180–200 nm and polydispersity indices of <0.1 determined using NanoSight technology suggest a monodisperse preparation of liposomes. Liposomes were inspected by cryoelectron microscopy to further validate the quality of the preparation (Fig. S2 A). CD spectroscopy revealed that the Opi1$^{111–128}$ peptide is unstructured in the presence of PA-free liposomes but adopts an α-helical conformation in the presence of PA-containing liposomes. The increased helicity of Opi1$^{111–128}$ at increased concentrations of PA in the liposomes (Fig. 2 A) suggests that the PA binding domain is unstructured in solution but folds into an AH upon PA-dependent membrane binding.

Given the overall similarity of the membrane-binding AH regions of Spo20 and Opi1 (Fig. S1, A and B), we performed a control experiment to test for PA selectivity of Opi1$^{111–128}$. Even when compensating for the maximally possible charge differences of the PA and PS headgroups, we found evidence for PA selectivity by Opi1. The helical content of the AH peptide (Opi1$^{111–128}$) was higher in the presence of liposomes with 20 mol% PA than in the presence of liposomes with 40 mol% PS (Fig. 2 A). This suggests that the AH of Opi1 has an inherent selectivity to PA, which is missing in the AH of Spo20 (Horchani et al., 2014).

Having shown that the isolated PA binding domain (Opi1$^{111–128}$) folds upon binding to PA-containing membranes, we aimed at determining the membrane recognition process also in the context of the Opi1 protein. To this end, we generated fusion constructs of MBP and Opi1 (full-length and C-terminal truncations) for the heterologous overproduction in *Escherichia coli*. After affinity purification of MBP-Opi1 (Fig. S2 B; Sreenivas and Carman, 2003; Loewen et al., 2004), we analyzed the oligomeric state of the fusion proteins by size exclusion chromatography (SEC; Fig. S2, C and D). Full-length MBP-Opi1 eluted as a higher oligomer in the void volume of a Superdex 200 column (Fig. 2 B). The truncation variant MBP-Opi1^{R180*} (predicted molecular weight, 63.3 kD) containing both the PA binding region and the functionally relevant leucine zipper motif (Opi1$^{139–160}$; Fig. 1 C; White et al., 1991) was found in a dynamic equilibrium between monomers and dimers as concluded form SEC–multiangle light scattering (MALS; protein molecular weight, ∼100 kD; Fig. S2 E), and SEC experiments performed with various concentrations of MBP-Opi1^{R180*} from 2 mg/ml to 0.25 mg/ml (Fig. S2 F). MBP-Opi1^{S114*} (55.9 kD) lacking the PA binding domain and the leucine zipper eluted as monomeric protein (Fig. 2 B). Based on these gel filtration experiments and the low copy number of Opi1 (Ghaemmaghami et al., 2003), we estimate that the majority of the cellular Opi1 is in a monomeric form. For binding assays, we used only the peak fraction from SEC experiments (Figs. 2 B and S2, C and D).

The membrane binding and lipid selectivity of Opi1 was investigated in vitro using liposome flotation (LF) assays (Fig. 2 C). MBP-Opi1^{R180*} was incubated in the presence of PC-based liposomes containing different molar fractions of PA or PS but exhibiting identical lipid acyl chain compositions. After flotation of the liposomes in a discontinuous sucrose gradient, four equal fractions were retrieved from the gradient and subjected to SDS-PAGE. The percentage of membrane-bound Opi1 in the top fraction was quantified by densitometry after Instant Blue staining, which marks proteins and lipids, thus providing a convenient way to validate a successful flotation of liposomes (Fig. 2 C). Consistent with our findings on the isolated PA-binding region

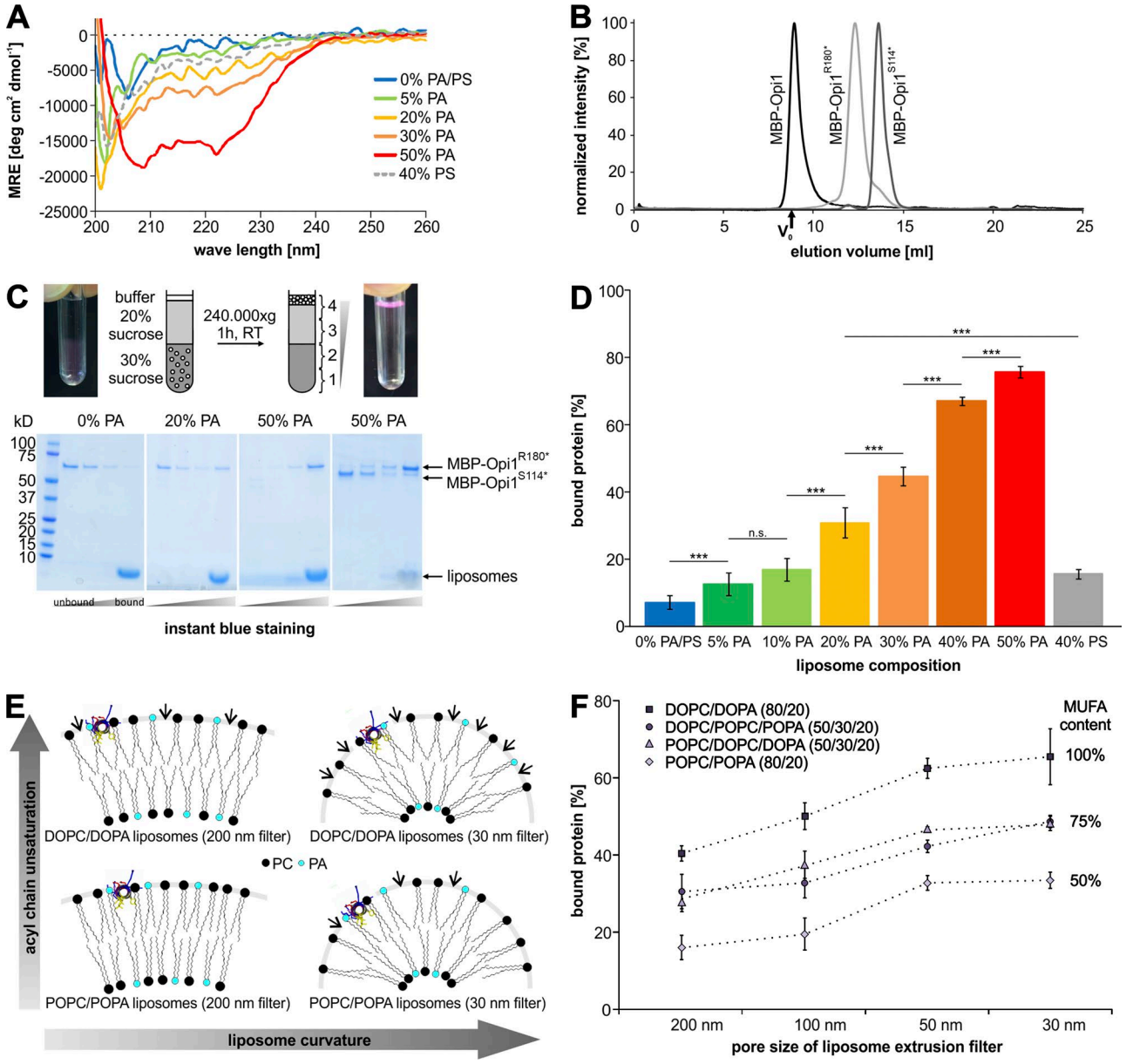

Figure 2. **The AH of Opi1 senses PA, lipid packing, and membrane curvature. (A)** CD spectral analysis of the Opi1$^{111–128}$ synthetic peptide in the presence of extruded PC-based liposomes containing different molar fractions of the indicated anionic lipids. **(B)** The indicated MBP-Opi1 fusion constructs were affinity purified and analyzed by SEC. The void volume (V_0) of the Superdex 200 Increase 10/300 column was 8.9 ml. **(C)** Indicated MBP-Opi1 variants were incubated with liposomes containing different PA concentrations. After LF, the discontinuous sucrose gradient was fractionated, and the samples were subjected to SDS-PAGE. **(D)** The liposome-bound fraction Opi1 was determined for the indicated liposomes in plotted in a bar diagram. Data points represent the average of three independent experiments except for the 0% PA/PS and 40% PS conditions (n = 9) and the 20% PA conditions (n = 11). Error bars represent SD. Asterisks indicate significant differences: ***, P < 0.01. **(E)** Schematic illustration of the impact of membrane curvature and the unsaturation degree of lipid acyl chains on the frequency of interfacial voids (arrows). **(F)** The binding of MBP-Opi1^{180*} to different liposomal preparations was analyzed. The proportion of monounsaturated lipid acyl chains (MUFA content) was varied by mixing the indicated lipids, and the liposomal diameter was modified by extrusion through filters with indicated pore sizes. Dashed lines highlight the role of membrane curvature. Data are given as average of at least three independent experiments with the error bars representing the SD.

(Opi1$^{111–128}$; Fig. 2 A), we found that membrane binding of MBP-Opi1^{R180*} increases with the molar fraction of PA (Fig. 2, C and D). MBP-Opi1^{S114*} lacking both the PA binding domain and the leucine zipper failed to bind to PA-containing liposomes (Fig. 2 C, right). The selectivity of Opi1 for PA- over PS-containing membranes was underscored by the observation that liposomes with 20 mol% PA bound Opi1 more efficiently than liposomes with 40 mol% PS (Fig. 2 D). Thus, even when compensating for the maximum possible difference of the headgroup charge per area of membrane, Opi1 favors binding to PA- over PS-containing membranes, strongly suggesting that it endows specific features for PA selectivity.

If Opi1 recognizes PA-containing membranes by folding an AH into the lipid bilayer, the membrane binding should be affected

by the membrane curvature and the molecular lipid packing density of the lipids. Interfacial membrane voids, also referred to as lipid packing defects, should facilitate the insertion of hydrophobic side chains into the core of the lipid bilayer and thus the folding of the AH (Drin and Antonny, 2010; Antonny, 2011). To test this, MBP-Opi1^{R180*} was incubated with liposomes containing 20 mol% PA but differing either in their membrane curvature or their acyl chain composition. The curvature of the liposomes was adjusted by stepwise extrusions through polycarbonate filters with decreasing pore sizes from 200 nm to 30 nm. The lipid compositions were chosen to yield different molar fractions of esterified monounsaturated fatty acids (MUFA content) from 50 mol% to 100 mol%. After floating the liposomes in a sucrose step gradient, the fraction of MBP-Opi1^{180*} cofloating with the liposomes was determined. The binding of MBP-Opi1^{180*} to liposomes was favored both by an increased membrane curvature and by an increased proportion of monounsaturated lipid acyl chains in the lipid bilayer (Fig. 2 F).

Despite structural differences to classical ALPS motifs (Drin and Antonny, 2010), the basic AH of Opi1 has a preference for positively curved and loosely packed membranes. Nevertheless, the sensitivity of Opi1 to these bilayer properties is more moderate than reported for ALPS motifs that exhibit a sharp increase of membrane binding at high membrane curvature (Drin and Antonny, 2010). This allows Opi1 to respond over a broader spectrum of membrane curvatures and lipid-packing densities (Fig. 2 F), which may be relevant for fine-tuning membrane biogenesis. The precise position of the saturated and the unsaturated lipid acyl chains, however, appeared irrelevant. When 20 mol% of POPA were substituted by 20 mol% 1,2-dioleoyl-*sn*-glycero-3-phosphate (DOPA) and compensated via the POPC and DOPC content to maintain the total acyl chain composition, the binding of MBP-Opi1^{180*} was only marginally affected, if at all (Fig. 2 F). Consistent with previous findings (Kassas et al., 2017), these data suggest that Opi1 senses not only the PA content but also a bulk membrane property related to the lipid acyl chain composition.

Interfacial hydrophobicity tuning of an AH modulates membrane binding

Having established that Opi1 uses an AH for membrane recognition, we set out to tune its properties by rational design. If the hydrophobic face of the AH contributed to membrane recruitment, an increase of the interfacial hydrophobicity should increase membrane binding, whereas a decrease should lower it. First, we focused on Y127, the residue with the highest interfacial hydrophobicity in the hydrophobic face of the Opi1 AH (Wimley and White, 1996). A Y127W mutation was generated to increase the hydrophobicity, whereas the mutations Y127A and Y127D were introduced to decrease it. As alternative approach, we introduced a G120W mutation in the hydrophobic face of the AH to increase both the hydrophobicity and the helical propensity (Wimley and White, 1996; Monné et al., 1999). We also increased the length of the AH by a simple duplication of the sequence from residue 114 to residue 131 (2× AH). These variants of MBP-Opi1^{R180*} (Fig. 3 A) were isolated (Fig. 3 B) and subjected to membrane-binding assays. The proportion of unsaturated lipid acyl chains was kept at 75% in all experiments, whereas the molar fraction of PA was varied between 0 and 50 mol% (Fig. 3, C–I). Liposomes containing 40 mol% PS were used to test whether changes in the hydrophobic face of the AH and the resulting possible changes in its positioning relative to the bilayer might contribute to the headgroup selectivity of Opi1 (Fig. 3 J). The binding assays revealed that none of the MBP-Opi1^{R180*} variants binds to liposomes with ≤5 mol% PA (Fig. 3, C and D). Consistent with earlier findings (Loewen et al., 2004; Young et al., 2010), this suggests that electrostatic interactions between the PA headgroup and basic residues of Opi1 (Fig. 1 D) are a prerequisite for membrane recruitment. However, the approach of tuning the AH by targeting its hydrophobic face was successful at intermediate PA levels of 10–30 mol% (Fig. 3, E–G): decreasing the interfacial hydrophobicity at position 127 by the Y127D and Y127A mutations weakened membrane binding of Opi1, whereas increasing the hydrophobicity by the Y127W exchange strengthened it (Fig. 3, E–G). The G120W mutation increases both the hydrophobicity and the helix propensity of the AH, making it even more effective than the Y127W mutation in supporting membrane recruitment of Opi1 as apparent from the experiments with liposomes containing 20 and 30 mol% PA (Fig. 3, F and G). Not surprisingly, the duplication of the AH turned out to be most effective in supporting membrane recruitment of Opi1 (Fig. 3, E–G). At higher levels of PA, Opi1 efficiently bound to the liposomes irrespective of the mutations introduced in the hydrophobic face of the AH (Fig. 3, H and I). Thus, the electrostatic interactions between the PA headgroup and basic residues in the AH can be dominant over the contribution of the hydrophobic face in mediating membrane binding. These experiments revealed further evidence for a PA selectivity of Opi1. For all of the tested variants of Opi1, the binding to liposomes containing 40 mol% PS (Fig. 3 J) was weaker than the binding to liposomes containing 20 mol% PA (Fig. 3 F). We conclude that the hydrophobic face of the AH can be tuned to modulate membrane binding at intermediate PA levels but does not critically contribute to PA selectivity.

Interfacial hydrophobicity tuning to control cellular signaling

The molar fraction of PA in total cell lipidomes has been reported to lie between 5 and 15 mol% depending on the growth conditions (Klose et al., 2012). Other research reported that PA makes up only 0.2–3% of the glycerophospholipids in isolated microsomal fractions from yeast (Zinser et al., 1991). Thus, it is clear that the cellular level of PA is typically lower than the 10–30 mol% of PA for which interfacial hydrophobicity tuning proved most efficient in vitro (Fig. 3, E–G). In cells, the ER network provides a high density of ER membranes unmatched by liposome-based in vitro experiments. Furthermore, Opi1 binding is stabilized by the ER membrane-spanning protein Scs2 interacting with the Opi1 FFAT motif as a coreceptor (Fig. 1 C; Loewen et al., 2003, 2004). Therefore, it is conceivable that a quantitative recruitment of Opi1 to the ER occurs already at lower levels of PA in vivo, which is also evident from fluorescence microscopy (Loewen et al., 2004). To validate our tuning approach in cells, we generated Opi1-mGFP knock-in constructs that were targeted to the endogenous gene locus of *OPI1*. Notably, the C-terminal tagging of Opi1 does not cause any profound functional defect (Gaspar et al., 2011). Building on our in vitro experiments (Figs. 2 and 3),

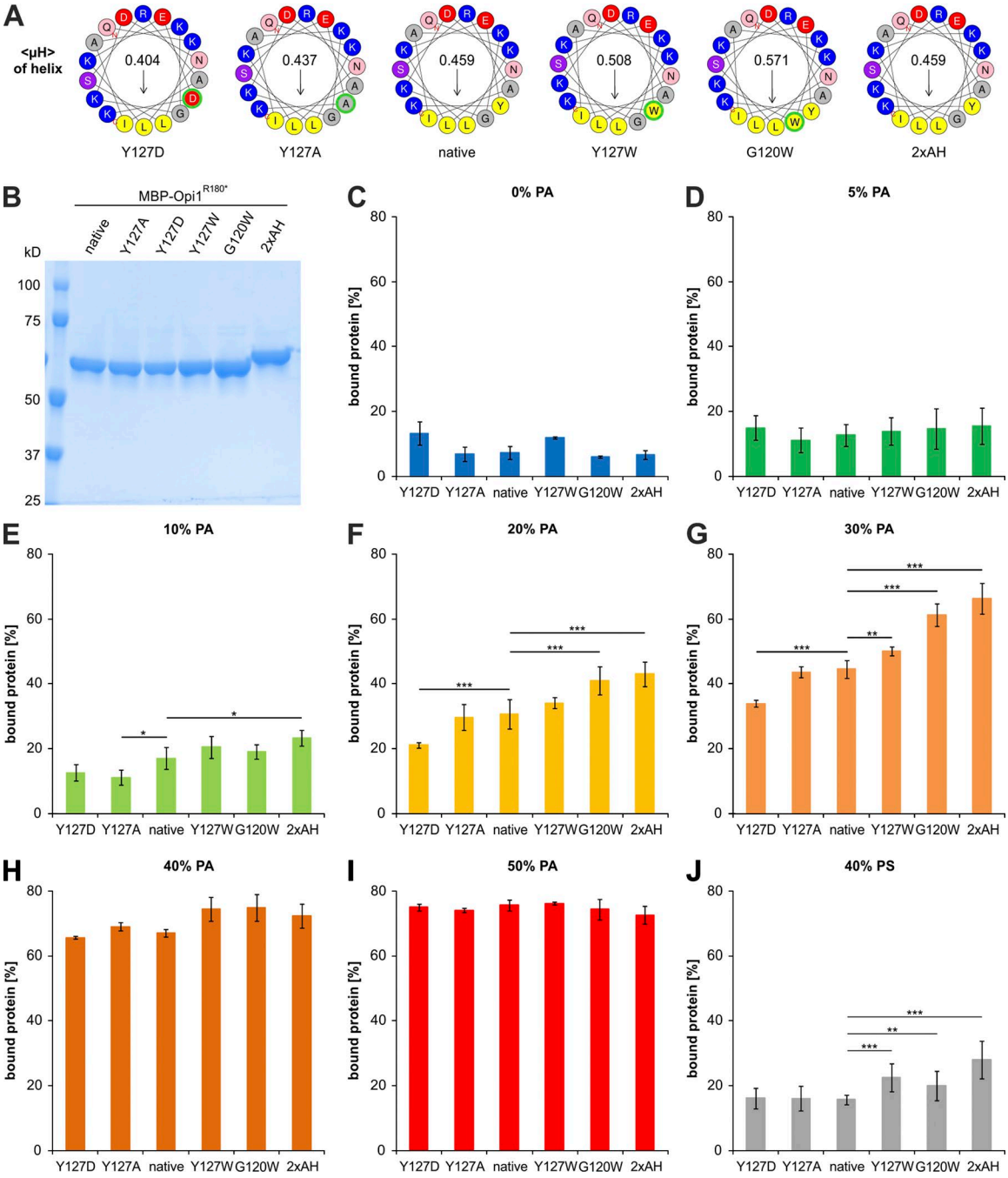

Figure 3. **Interfacial hydrophobicity tuning affects membrane binding of MBP-Opi1^{R180*}. (A)** Helical wheel representations of different MBP-Opi1^{R180*} variants using HeliQuest. **(B)** The indicated MBP-Opi1^{R180*} variants were purified by a two-step purification protocol. 1 µg of each protein was subjected to SDS-PAGE for quality control. **(C–J)** Opi1 binding assays to liposomes containing increasing proportions of POPA (C–I) or 40 mol% POPS (J) as performed for Fig. 2 C. The data show the average of two (C, H, and I) and three (D–G and J) independent experiments. Values for the native MBP-Opi1^{R180*} variant with 0% PA, 20% PA, and 40% PS are derived from 9, 11, and 9 independent experiments, respectively, and are identical to the data represented in Fig. 2 D. Error bars represent SD. Asterisks indicate significantly perturbed binding compared with the native protein variant: *, P < 0.1; **, P < 0.05; ***, P < 0.01. Significance tests were not conducted for C, H, and I (n = 2).

we generated a series of Opi1-mGFP variants by tuning the interfacial hydrophobicity of the AH. Aiming at the disruption of the amphipathic character of the PA binding domain, we generated three mutant variants: Y127R, Y127K, and Y127D. A Y127A mutation was generated to test whether the mild membrane binding defect of Opi1 observed in vitro (Fig. 3 E) would be detectable by sensitive cell-based assays also in vivo. To test whether an aromatic residue at position of Y127 is specifically required for normal signaling, we generated a Y127L mutation featuring a similar interfacial hydrophobicity (Wimley and White, 1996) while lacking the aromatic character. The G120W and the G120W/Y127A mutations were generated to cover a broader spectrum of interfacial hydrophobicities in the AH. Finally, the ΔNLS mutant (Opi1$^{KRQK->AAQA}$) lacking the nuclear localization sequence served

as an additional control. These rationally designed variants of Opi1 were subjected to an in-depth phenotypic characterization: (i) inositol auxotrophy on solid media identified mutations that destabilize the binding of Opi1 to the ER (Fig. 4 A), (ii) live-cell confocal microscopy provided complementary information on the subcellular localization of Opi1-mGFP variants (Fig. 4 B), (iii) the cellular growth rate in liquid medium during acute inositol depletion provided an indirect yet quantitative measure for defective membrane recruitment of Opi1 (Fig. 4 C), and (iv) the overproduction of inositol (Opi$^-$) phenotype identified Opi1 mutant variants that are stabilized at the ER, thereby causing a deregulated *INO1* expression and inositol secretion from the cell. Secreted inositol can be detected by an inositol auxotrophic tester strain forming a red halo around a spotted inositol-secreting colony on an otherwise inositol-free plate (Fig. 4 C, middle; Greenberg et al., 1982). An immunoblot to detect the steady-state level of the generated Opi1-mGFP variants served to complement the phenotypic characterization. As the *OPI1* promoter contains a UAS_{INO} sequence, it is repressed by the *OPI1* gene product itself (Schüller et al., 1995), and the steady-state level of Opi1-mGFP should correlate with the strength of membrane binding of the engineered Opi1 variants (Fig. 4 C). Using this palette of phenotypic readouts, we studied the responsiveness of the Opi1 regulatory system to characterize rationally designed AH variants in living cells (Fig. 4, A–C).

All mutant variants showed normal growth on solid media plates containing inositol (Fig. 4 A), whereas the disruption of the amphipathic character by the Y127K, Y127R, and Y127D mutations and a decreased interfacial hydrophobicity by the Y127A mutation caused significant growth defects on media lacking inositol, especially at an elevated growth temperature (Fig. 4 A). Consistently, the localization of mutant Opi1-mGFP was greatly affected during acute inositol depletion, which is known to cause an increase of the cellular level of PA (Fig. 4 B; Hofbauer et al., 2014). Although the native Opi1-mGFP localized to the ER under these conditions, the Y127K, Y127R, Y127D, and less so the Y127A showed an increased nuclear localization, suggesting a failure of these mutants to bind PA at the ER membrane. As these Opi1-mGFP variants cannot activate membrane biogenesis even during a buildup of PA, the respective cells show profound growth defects during prolonged phases of inositol depletion (Fig. 4 C). Immunoblotting for Opi1-mGFP from cellular lysates revealed reduced steady-state levels of the Y127R, Y127K, Y127D, and Y127A variants compared with native Opi1-mGFP (Fig. 4 C). This suggests that the increased nuclear localization of these mutants represses the *OPI1* gene, resulting in decreased steady-state protein levels. Thus, all mutants disrupting the AH and lowering its interfacial hydrophobicity also disrupt Opi1 binding to the ER and lead to growth defects during inositol depletion. Intriguingly, the substitution of Y127 with basic residues (Y127R and Y127K) caused milder growth defects than the Y127D mutation (Fig. 4, A and C). This may indicate that these basic side chains can "snorkel" toward the aqueous environment (Öjemalm et al., 2016) and rescue membrane recruitment by providing additional electrostatic interactions with the PA lipid headgroups.

The rational design of the AH also led to Opi1-mGFP variants with enhanced membrane-binding properties. Whereas the Y127L variant appeared most similar to native Opi1-mGFP in all assays, the G120W/Y127A and the G120W variants were better binders. Cells expressing these variants neither exhibited growth defects in inositol-lacking media (Fig. 4, A and C) nor did these Opi1 variants show an aberrant localization compared with the native form during inositol depletion (Fig. 4 B). Instead, the increased ER membrane binding of these mutants led to the secretion of inositol as indicated by Opi$^-$ phenotypes (Fig. 4 C). This was most pronounced for the ΔNLS variant (Opi1$^{KRQK->AAQA}$) that cannot enter the nucleus because of a missing nuclear localization sequence (Fig. 4 C). These data suggest a dynamic distribution of Opi1 between two compartments: at the ER membrane and in the nucleus (Loewen et al., 2004). The increased binding of the G120W/Y127A, G120W, and ΔNLS variants to the ER membrane also caused a derepression of *OPI1* and consequently an increased steady-state cellular level of Opi1 (Fig. 4 C). Thus, rational design of interfacial hydrophobicity is suitable to tune Opi1's membrane binding, its subcellular localization, and its regulatory functions.

Based on the shape and size of the GFP-positive signal in cells (as in Fig. 4 B), we established a localization index that allowed us to quantitatively assess the impact of interfacial hydrophobicity tuning on the subcellular localization of Opi1-mGFP. The automated analysis established a ranking of the disruptive mutations (Fig. 4 D). The binding of Opi1 variants to the ER increases in the order—Y127D < Y127R < Y127K < Y127A < native—and the stabilizing variants can be ranked from weaker binders to better binders as native < Y127L < G120W/Y120A~G120W (Fig. 4 D). We further corroborated these findings in diploid cells by two-color confocal microscopy: simultaneous imaging of native Opi1 fused to an RFP (Opi1-mRFP) and tuned variants fused to mGFP by confocal microscopy validated a perturbed subcellular localization of the tuned variants (Fig. S3 A). The subcellular localization of the different Opi1-mGFP variants was greatly affected by mutations in the AH, whereas the native Opi1-mRFP remained predominantly associated with the ER membrane. Thus, even though Opi1 can form dimers as shown in vitro (Figs. 2 B and S2, E and F), its subcellular localization is dominated by the AH interacting with cellular membranes and not by an association with a second, native Opi1 variant. In summary, we conclude that interfacial hydrophobicity tuning affects subcellular Opi1 directly and not via indirect, secondary effects such as an altered ER lipid composition.

Our data establish the tuning of interfacial hydrophobicity as a promising tool for custom-designing membrane recruitment of proteins. To challenge this proposal, we tested whether a rationally designed Opi1^{G120W}-mGFP variant with an increased in vitro membrane-binding potential (Fig. 3, F and G) could compensate for a loss of Scs2, the coreceptor for Opi1 at the ER membrane. The loss of Scs2 causes significant growth defects on media lacking inositol, especially at elevated temperatures (Fig. 4 E; Loewen et al., 2003; Gaspar et al., 2017). These effects are phenocopied by a mutation in the Opi1 FFAT motif (Opi1^{D203A}-mGFP) that disrupts the interaction between Opi1 with Scs2 (Fig. 4 E; Loewen and Levine, 2005). Strikingly, the G120W mutation in Opi1 is sufficient to rescue the inositol auxotrophy associated with a loss of Scs2 (Fig. 4 E) by recruiting Opi1 to membrane structures associated with lipid droplets (Fig. S3 B), and it causes a mild Opi$^-$ phenotype even in an *scs2* background

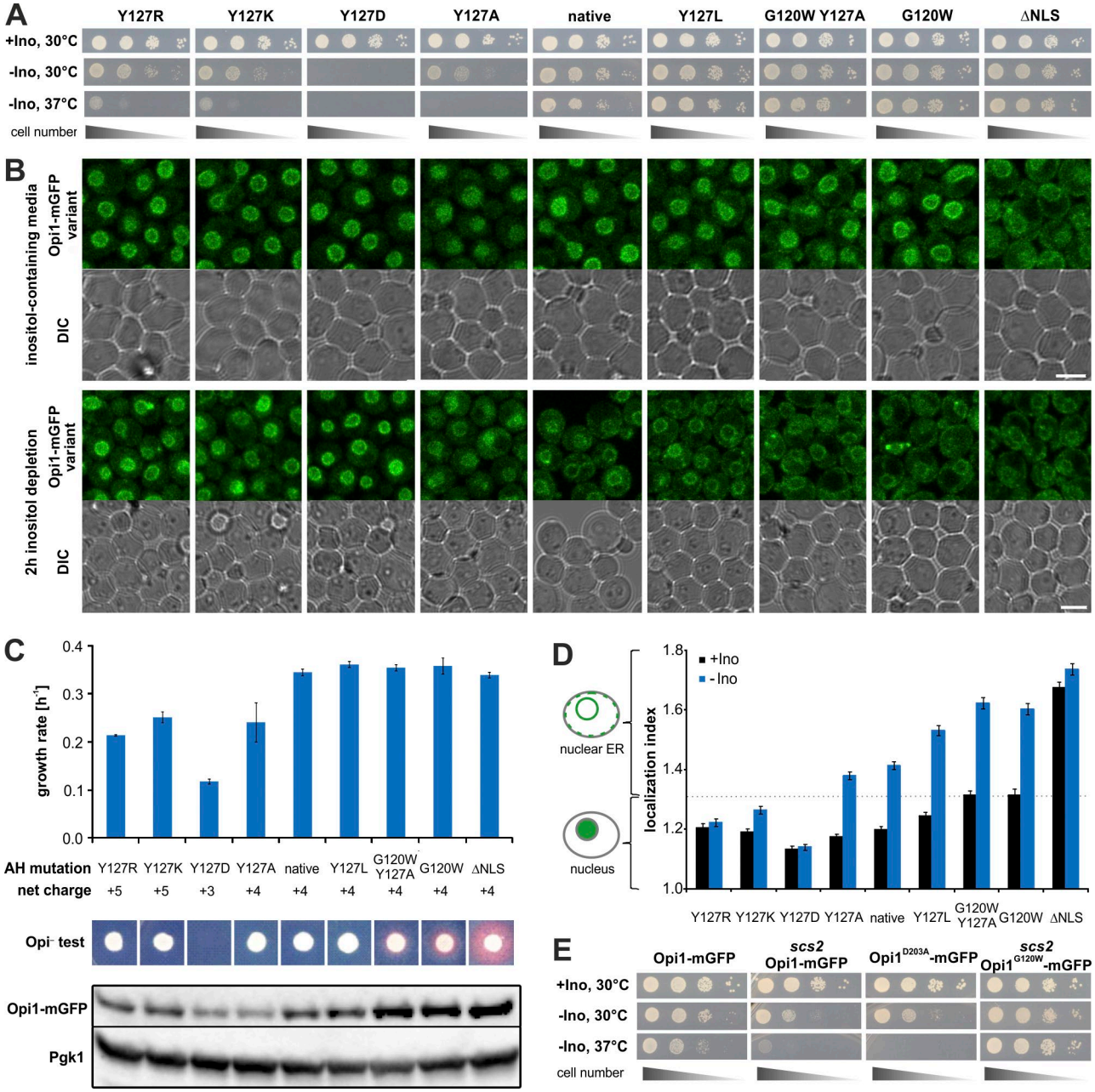

Figure 4. **In vivo validation of interfacial hydrophobicity tuning. (A)** Chromosomally integrated Opi1-mGFP variants were spotted on solid media either containing (+Ino) or lacking inositol (−Ino) at the indicated temperatures and scanned after 2 d cultivation. **(B)** Representative micrographs of live cells expressing Opi1-mGFP variants cultivated on inositol-containing liquid media or for 2 h after inositol depletion. Bars, 5 µm. DIC, differential interference contrast. **(C)** Phenotypical characterization of the indicated Opi1-mGFP variants. The average growth rate in liquid medium lacking inositol between 3 and 6 h inositol depletion from three independent experiments is plotted with the error bars representing the SD. The Opi$^-$ phenotype was used to monitor secretion of inositol apparent as a red halo around a spotted colony. Steady-state levels of the MBP-Opi1^{R180*} variants in the lysates of cells cultivated for 2 h in inositol-lacking media were analyzed by immunoblotting. Opi1-mGFP was detected using an anti-GFP antibody with anti-Pgk1 antibody as internal control. **(D)** Automated quantification of micrographs from B. The localization index is a semiquantitative measure for the subcellular localization of the indicated Opi1-mGFP variants. A localization index <1.3 indicates a nuclear localization, and a localization index >1.3 indicates ER localization. The data points are based on four independent replicates with >190 cells analyzed per strain. The error bars represent SD. **(E)** Viability assay of chromosomally integrated Opi1-mGFP variants in WT and *scs2* deletion strain backgrounds. Plates were scanned after 2 d growth on solid media at the indicated temperatures.

(Fig. S3 C). Importantly, a localization of the native Opi1 to PA-enriched subdomains of the nuclear ER in conjunction with lipid droplet formation has previously been reported (Grippa et al., 2015; Wolinski et al., 2015). Thus, a point mutant in the AH of Opi1 can compensate for the loss of the Scs2 coreceptor in the ER membrane.

Identification of a structural motif for PA selectivity

Opi1 is selective for PA over PS (Figs. 2 and 3). We used multiresolution MD simulations to gain insight into the mechanism of selective PA recognition. We modeled an Opi1$^{111–132}$ peptide as an α-helix and created two different systems including the

AH, solvent, and lipid bilayers containing either 20 mol% PA or 20 mol% PS for coarse-grained (CG) MD simulations using the MARTINI representation (Marrink et al., 2007; de Jong et al., 2013). Both lipid bilayers were composed of 60 mol% POPC, 20 mol% DOPC, and either 20 mol% DOPA or 20 mol% DOPS to yield bilayers with 70% monounsaturated acyl chains. After initial CG simulations allowing the Opi1 peptide to associate spontaneously and equilibrate with the membrane, each system was lifted from the CG representation to a fully atomistic representation in the CHARMM36 force field (Jo et al., 2007, 2008, 2009, 2014; Wassenaar et al., 2014; Lee et al., 2016). We simulated both the PA and PS membrane systems for 10 µs, during which the AH remained stably associated with the respective lipid bilayer (Fig. 5, A and B). All lipid species were mobile and exchanged between regions close to the AH peptide and the bulk membrane. The hydrophobic residues of the AH pointed into the hydrophobic core of the bilayer, whereas the hydrophilic residues were situated in the membrane water interface (Fig. 5, A and B).

We identified structural features of particular importance for the binding of PA and PS from the localization probability of these lipids relative to the AH peptide (Fig. 5, C and D). We found that the AH attracts and enriches both PA and PS in its vicinity (Fig. 5, C and D) but not DOPC and POPC (Fig. S4, A and B). This local enrichment of anionic lipids occurred only in the membrane leaflet containing the AH peptide and was absent in the opposing leaflet of the lipid bilayer (Fig. S4, A and B). Notably, PA and PS were concentrated at discrete hotspots of binding: in the proximity of the KRK motif formed by K112, R115, and K119 and the 3K motif formed by K121, K125, and K128, pointing in the opposite directions from the AH (Fig. 5 B). The PA and PS binding hotspots differed in their position and distance relative to the KRK and 3K motifs. These differences are not caused by different charges in the lipid headgroup region as the net charge was maintained at –1 for both lipids throughout the simulations.

To further characterize these different modes of binding, we prepared an MD simulation with a mixed bilayer containing both 20 mol% PA and 20 mol% PS with the headgroup charges maintained at –1. Strikingly, the binding of PA to the KRK and the 3K motif prevented an accumulation of PS in the vicinity of the AH (Fig. 5, E and F), suggesting that PA binding dominates over PS binding. The distance profile of PA and PS relative to the KRK (Fig. 5 G) and 3K motifs (Fig. 5 I) revealed populations of PA lipids interacting preferentially with these two basic motifs distances between 4 and 6 Å (Fig. 5, G and I). Neither PS (Fig. 5, G and I) nor PC (Fig. S4, D and E) lipids formed such a population and were found only at greater distances, thereby suggesting a strong and specific mode of PA binding at the two binding motifs. This interpretation is further supported by the lipid residence times in the proximity of both motifs (Fig. 5, H and J). Although the details of the binding kinetics are challenging to establish because of the relatively slow exchange of lipids, we observed that PA lipids dwell longer close to the 3K motif than PS or PC lipids (Fig. 5 J). Our atomistic MD simulations therefore suggest that the AH of Opi1 interacts more intimately and stably with PA than with PS or PC lipids. A closer inspection of the trajectories revealed that the phosphate moiety of PA can be enwrapped by the three basic residues of the 3K motif, forming a three-finger grip (Fig. 5 K), which fail to accommodate the larger PS headgroup (Fig. 5 L). Overall, the atomistic MD simulations indicate that both the KRK motif and the 3K motif have substantially higher affinity for PA than for PS.

Tuning lipid selectivity by rational design

Having identified a putative mechanism for PA selectivity by MD simulations, we set out to validate this finding experimentally. The AH of Opi1 contains two acidic residues and several basic residues, possibly forming two PA-selective three-finger grips (Fig. 5 B). We wondered whether PA selectivity may be assisted by the specific arrangement of attractive and repelling forces brought about by basic and acidic residues in the hydrophilic face of the AH. As an alternative but not mutually exclusive model, we speculated that a PA-selective three-finger grip, which relies on just three basic residues on one side of an AH, may have specific structural requirements for efficiently enwrapping the PA headgroup. Thus, the substitution of the lysine-rich AH to an all-arginine AH was expected to affect PA selectivity resulting from the steric differences between arginine and lysine side chains that might prevent the formation of a tight-fitting three-finger grip. Moreover, because the guanidinium group of arginine can form multiple hydrogen bonds with water and the polar lipid headgroups (Li et al., 2013), we reasoned that an all-arginine AH might not be able to efficiently distinguish between PA and other anionic glycerophospholipids. We thus generated an MBP-Opi1^{R180*} D122K/E126K variant to increase the net charge of the AH from +4 to +8 and a second variant in which all lysine residues of the AH were replaced by arginines (5K5R), therefore not changing the net charge of the AH (Fig. 6 A).

After isolation of the indicated MBP-Opi1^{R180*} variants by affinity purification and SEC (Fig. 6 B), we characterized their binding to PA- and PS-containing liposomes using LF assays (Fig. 6 C). The PA-containing liposomes were composed of 50 mol% DOPC, 30 mol% POPC, and 20 mol% POPA, whereas PS-containing liposomes were composed of 50 mol% DOPC, 10 mol% POPC, and 40 mol% 1-palmitoyl-2-oleoyl-*sn*-glycero-3-phospho-L-serine (POPS) to compensate for the possible charge differences in the headgroup region. Liposomes composed solely of 50 mol% DOPC and 50 mol% POPC served as negative control (Fig. 6 C). The D122K E126K mutant with a net charge of +8 showed an increased membrane binding to both PA- and PS-containing liposomes, suggesting that increased electrostatic interactions between the AH and anionic lipids supports membrane binding and that the acidic residues have only a minor—if any—function for PA selectivity. Notably, the 5K5R mutant lost the preference for PA- over PS-containing liposomes. Although cells expressing these mutants show normal growth on inositol-depleted medium (Fig. S5 A) and a normal subcellular localization (Fig. S5 B), they exhibit a significant Opi$^-$ phenotype (Fig. S5 C), which is consistent with an increased strength of membrane binding. MD simulations of the 5K5R mutant in bilayers containing equal molar concentrations of PA and PS (Fig. 6, D and E; and Fig. S5 D) identify a large increase in affinity of PS to arginines at the 3K site, which

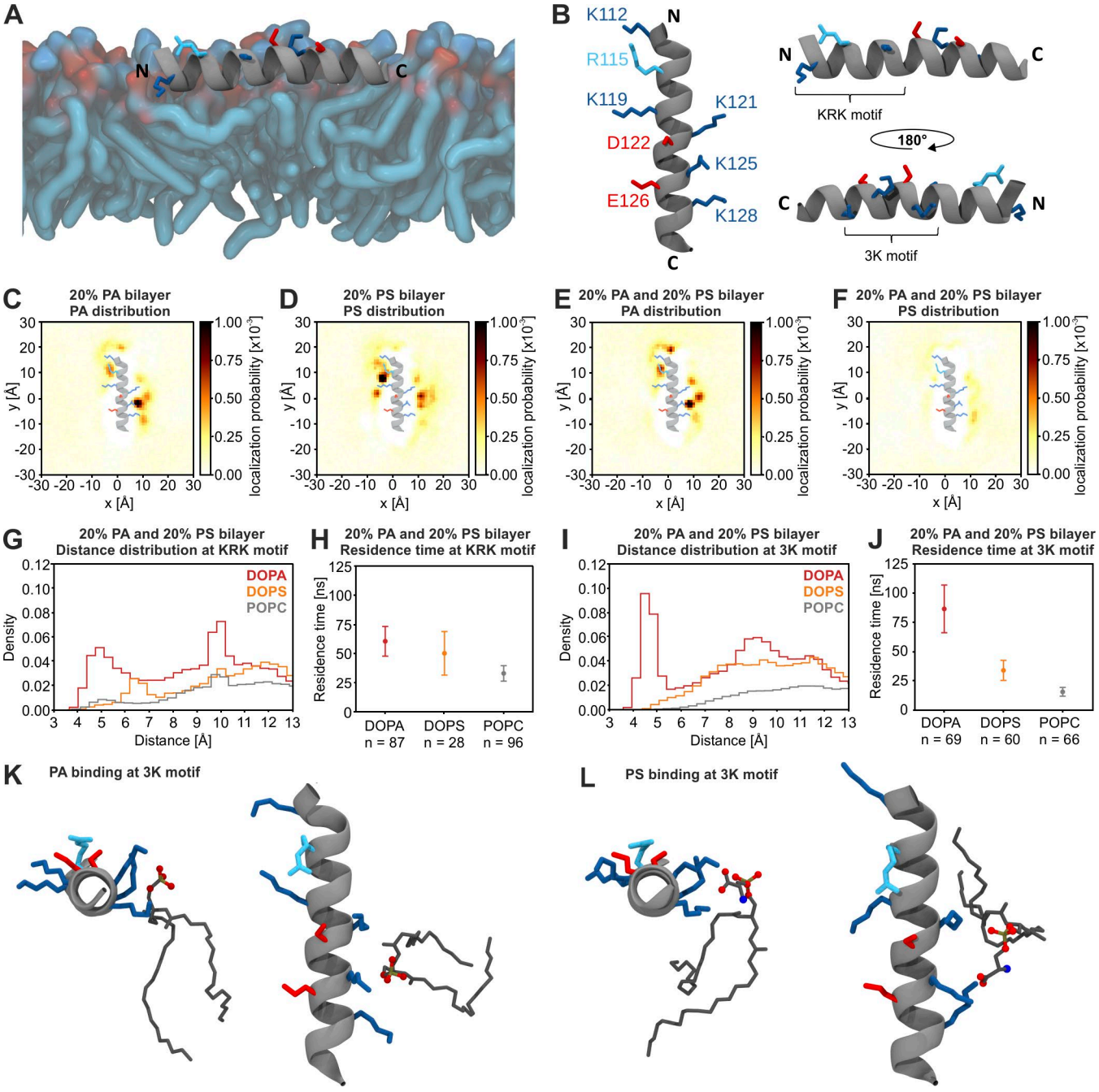

Figure 5. **MD simulations of PA and PS binding to Opi1 AH. (A)** Representative structure of the AH of Opi1$^{120–132}$ in a lipid bilayer from an all-atom MD simulation. The helix is represented as a gray ribbon with lysine (blue), arginine (cyan), and aspartate and glutamate (red) sidechains as sticks. Lipids are shown as tubes (carbon, blue; oxygen, red). Only the top membrane leaflet is shown. **(B)** Representative structure of Opi1 AH (Opi1$^{120–132}$) from three perspectives: from top (left), from the N to C terminus (top right), and from the C to N terminus (bottom right). The three-finger grip forming KRK and 3K motifs are indicated. **(C–F)** Time-averaged positions of the phosphate moieties from two lipid species (C and E, DOPA; D and F, DOPS) in three different all-atom MD simulations (C, 20% PA; D, 20% PS; E and F, mixed 20% PA/20% PS) performed for 10 µs each. Colors indicate the localization probability of a lipid over the course of the trajectory. DOPA lipids localize closer to the 3K motif (C) than DOPS lipids (D). DOPA displaces DOPS in a mixed bilayer at both motifs (E and F). The Opi1 AH was superimposed to highlight the hotspots of lipid binding. **(G–J)** Distribution of pairwise distances and residence times calculated from a lipid-binding motif and the lipids present in a mixed bilayer. DOPA (red) is found closer to the AH than DOPS (orange), and POPC (gray) was found for both the KRK motif (G) and the 3K motif (I). The residence time of PA at the 3K motif was significantly longer than that of PS (J). The number of observed binding events (H and J) is indicated as a label on the x axis, and error bars represent SD. **(K and L)** Representative structures of a DOPA (K) or DOPS (L) lipid interacting with lysines at the 3K motif shown from the C terminus (left) and top view (right). DOPA interacts with oxygens of the phosphate moiety. DOPS interacts also with the carbonyl oxygens of serine, keeping it at a larger distance from the AH.

was virtually absent for the native AH peptide (Figs. 5 F and 6 E). Thus, MD data and experimental evidence suggest that the AH of Opi1 exhibits an inherent selectivity for PA, which is abolished in the 5K5R mutant. The physiological relevance of the PA selectivity by Opi1 is illustrated by an Opi$^-$ phenotype of the 5K5R mutant (Fig. S5 C).

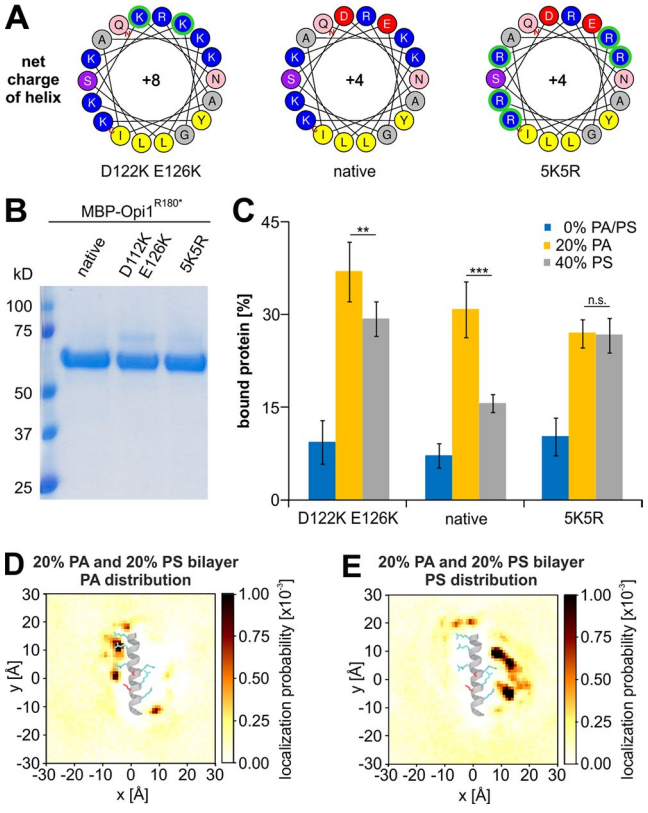

Figure 6. **The hydrophilic face of Opi1´s AH is crucial for lipid headgroup selectivity. (A)** Helical wheel representation of MBP-Opi1^{R180*} variants using HeliQuest. **(B)** The indicated MBP-Opi1^{R180*} variants were purified by a two-step purification. 1 µg of each protein was subjected to SDS-PAGE for quality control. **(C)** Liposome-binding assays with the indicated MBP-Opi1R180* variants were performed as in Fig. 2 C. The bar diagrams show the average of five independent experiments for the D112K E126K mutant and three independent experiments for the 5K5R mutant. Values for the native MBP-Opi1^{R180*} variant with 0% PA, 20% PA, and 40% PS are the average of 9, 11, and 9 independent experiments, respectively, and are the same as in Fig. 2 D and Fig. 3 (C, F, and J). Error bars represent SD. Asterisks indicate significant differences: **, $P < 0.05$; ***, $P < 0.01$. **(D and E)** Time-averaged positions of phosphate head groups from different lipid species (DOPA, DOPS, DOPC, and POPC) relative to 5K5R AH in MD simulations performed for 2.4 µs and represented as in Fig. 5 (C–F).

Discussion

Cells must adjust their lipid metabolism to the available pool of nutrients in order to maintain membrane integrity in response to metabolic challenge or environmental cues. Membrane biogenesis relies on the coordinated regulation of lipid biosynthetic genes and enzymes and is under tight control of the transcriptional repressor Opi1 in *S. cerevisiae* (Schuck et al., 2009; Henry et al., 2012). The identification of an AH in Opi1 (Figs. 1, 2, and 3) provides a conceptual framework for the previous observations that Opi1 binding to the ER is controlled by the abundance of PA (Loewen et al., 2004), the lipid headgroup composition (Young et al., 2010; Putta et al., 2016), the intracellular pH (Young et al., 2010), the acyl chain length (Hofbauer et al., 2014), the degree of lipid unsaturation (Fig. 2 F; Kassas et al., 2017), and membrane curvature (Fig. 2 F; Kassas et al., 2017). Tuning the interfacial hydrophobicity reveals a significant and important contribution of the hydrophobic side of the AH to the membrane-binding strength both in vitro and in vivo (Figs. 3 and 4). The relatively low-affinity of Opi1's AH to PA-containing membranes as compared with the AH of Spo20 may reflect the sensor function of Opi1: to signal a low PA level in the ER, Opi1 must be able to detach easily from the ER membrane to repress lipid metabolic genes in the nucleus. Most probably, this is facilitated by the relatively low net charge in the AH region (Fig. S1, A and B) and the helix-destabilizing residue G120 (Figs. 3 and 4).

Analogous to ALPS motif containing proteins such as GMAP-210 or ArfGAP (Antonny, 2011), Opi1 senses the molecular packing density of lipids by folding an AH into the ER membrane; however, it responds to these changes of the bilayer more moderately and over a broader spectrum (Fig. 2 F). Thus, the Opi1 regulatory circuit integrates two crucial metabolic input parameters: the PA abundance and the lipid-packing density as a proxy for the lipid acyl chain composition. This feature may have a crucial role in maintaining membrane homeostasis in the stressed ER. Aberrant lipid compositions of the ER membrane can cause ER stress and activate the unfolded protein response (UPR; Walter and Ron, 2011; Halbleib et al., 2017). Perhaps the most prominent condition of lipid bilayer stress is an increased proportion of saturated lipids (Pineau et al., 2009; Deguil et al., 2011; Kitai et al., 2013; Surma et al., 2013). Under this condition, however, UPR activation initiates a detrimental positive feedback loop. Enforced membrane biogenesis controlled by the UPR causes a rapid consumption of coenzyme A–activated fatty acids, thereby depleting the substrates of the fatty acid desaturase Ole1 (Ballweg and Ernst, 2017). Consequently, the UPR activation by saturated lipids aggravates the stress-inducing condition and leads to severe changes of organelle morphology (Schneiter and Kohlwein, 1997; Surma et al., 2013). Intriguingly, this vicious circle has also been implicated in the decay of pancreatic insulin-producing β cells in the context of the metabolic syndrome (Cunha et al., 2008; Clark and Urano, 2016). By sensing the molecular lipid-packing density of the ER membrane, Opi1 provides a means to interrupt the vicious circle. An increased lipid-packing density would destabilize the binding of Opi1 to PA at the ER membrane. Once released, Opi1 would translocate to the nucleus and dampen membrane lipid biosynthesis to prevent the production of more saturated lipids. In this way, Opi1 counteracts lipid bilayer stress caused by saturated membrane lipids. It is tempting to speculate that Opi1 and the inositol-requiring enzyme Ire1, the most ancient and conserved UPR transducer, are part of an integrated regulatory circuit to control ER abundance. The fact that inositol is a key regulator of both Ire1 and Opi1 might be more than coincidence, pointing to a possible autoregulatory crosstalk between two major regulatory pathways of membrane biogenesis. This view is consistent with previous observations that Opi1 and Ire1 jointly regulate the abundance of the ER and that loss of Opi1 alleviates ER stress by increasing membrane biogenesis (Schuck et al., 2009; Velázquez et al., 2016).

Using the Opi1 regulatory system as a phenotypic showbox, we established interfacial hydrophobicity tuning as an approach to rationally design the membrane-binding strength of Opi1. This straightforward strategy is likely applicable to other membrane-binding AHs that are frequently found in enzymes and regulators of lipid metabolism (Puth et al., 2015), tethering

proteins of the secretory pathway (Magdeleine et al., 2016), and in antimicrobial peptides (Shai, 1999).

The mechanism of PA selectivity established by the three-finger grips in Opi1 (Fig. 5 K) is not mutually exclusive with the electrostatic/hydrogen bond switch model (Kooijman et al., 2005; Young et al., 2010), which proposes a second deprotonation of the phosphate moiety of PA for tightening the interaction. In fact, we find evidence that electrostatics are important contributors to membrane binding but also show that headgroup selectivity is accomplished by synergistic, structural means (Fig. 6, C–E).

A growing number of PA- and PS-binding proteins have been identified, and yet no structural element for a selective recognition of PA lipids has emerged (Stace and Ktistakis, 2006). In this study, we identify three-finger grips for PA binding (Fig. 5) based on two sequence motifs (KhXRhhhK and KXXhKXhK, where X stands for any and h for a hydrophobic amino acid) in the AH of Opi1 (Figs. 1 and 2). We are convinced that variations to this theme are common to install lipid headgroup selectivity in the AHs of membrane-binding proteins. Our MD simulations establish molecular details of PA recognition: PA is tightly enwrapped by three basic residues and binds more stably than PS or PC (Fig. 5 J). The loss of selectivity upon the substitution of lysine to arginine residues indicates that electrostatics is not the dominant factor (Fig. 6). The subtlety of these interactions helps us rationalize the observations that Opi1 but not Spo20 localizes to PA-enriched subdomains of the nuclear ER upon lipid droplet formation (Grippa et al., 2015; Wolinski et al., 2015).

Although the precise placement of the AH in the bilayer may be critical, we expect that similar structural elements also contribute to lipid headgroup selectivity and organelle-specific targeting of other proteins. The protein-tyrosine phosphatase SHP-1, for example, is activated by PA but not PS (Frank et al., 1999) and does indeed contain three-finger grip motifs. For predicting PA selectivity in a putative sensor protein, we need a better understanding of the nonequivalent functions of arginine and lysine during membrane adsorption and desorption. Importantly, membrane-active amphipathic peptides can have selective cytotoxic, antibacterial, or antifungal functions, and a nonequivalency of arginines and lysines for these functions is well established (Findlay et al., 2010; Jin et al., 2016; Liu et al., 2016). This work provides a new perspective to this nonequivalency by identifying a specific function of lysine side chains for lipid headgroup selectivity of an AH. We have shown that lipid headgroup selectivity of AHs has important implications for the regulation of lipid metabolism in yeast and may provide a new perspective to organelle-specific targeting of AH-containing proteins and to the inner workings of membrane-active antimicrobial and antifungal peptides.

Materials and methods

Reagents

If not stated otherwise, all reagents used in this study were of analytic grade and purchased from Sigma-Aldrich or Roth. The following lipids were purchased from Avanti Polar Lipids: DOPA (840875), POPA (840857), DOPC (850375), POPC (850457), and POPS (840034). The amylose resin was purchased from New England Biolabs, Inc., and the yeast nitrogen base (without amino acids and inositol), the complete supplement mixture, and agar were purchased from ForMedium. *E. coli and S. cerevisiae* strains used in this study are listed in Table S1, plasmids are listed in Table S2, and primers are listed in Table S3.

Peptide synthesis

The synthetic biotinylated Opi1$^{111\text{-}128}$ peptide (biotin QKLSRA IAKGKDNLKEYK-CONH$_2$; molecular weight, 2315.87 g/mol) was purchased from ZIK B CUBE (Technische Universität Dresden) and purified to >90% purity. The quality of the isolated peptide was validated by the supplier using mass spectrometry. The peptide was dissolved in NaPi buffer (20 mM sodium phosphate and 150 ml NaCl, pH 7.4) to yield a stock concentration of 10 mg/ml (4.3 mM) for further analyses.

Preparation and characterization of synthetic liposomes

Glycerophospholipid powders were dissolved in chloroform to yield 20 mg/ml stocks. The desired lipid compositions were mixed in 15 ml Pyrex glass tubes, dried under a steam of nitrogen, and incubated in an exsiccator with applied vacuum overnight to evaporate residual organic solvent. Lipid films were rehydrated for 2 h at room temperature using NaPi buffer (20 mM sodium phosphate and 150 mM NaCl, pH 7.4) to a final lipid concentration of 4 mM and mixed every 15 min. After rehydration, liposomes were subjected to five freeze/thaw cycles using liquid nitrogen and a 50°C heating block. Stepwise extrusion of these liposomes using the LipoFast extruder (Avestin) with 21 passages through pore size filters of 200, 100, 50, and 30 nm (Avanti Polar Lipids) yielded monodisperse populations of mostly unilamellar vesicles. The average size of the liposomes was determined using a NanoSight LM10 nanoparticle analysis system (Malvern Instruments). The measurements all contained at least 2,000 valid tracks, and the polydispersity index was <0.1 in all cases. The quality of the liposome preparation was further analyzed using cryoelectron microscopy. For plunge freezing, 3.5 µl sample was pipetted onto a glow-discharged Quantifoil 3.5/1 grid (Quantifoil) and vitrified using a Vitrobot (FEI) operated at a −1 offset and 4 s blotting time with prewetted filter paper (grade 595; Whatman). Cryogrids were imaged with a Tecnai F-30 (FEI) electron microscope operated at 300 kV. Images were recorded on a US4000 charge-coupled device camera (Gatan).

CD spectroscopy

Changes of the secondary structure of the synthetic Opi1$^{111\text{–}128}$ peptide was measured using a Jasco J-810 spectropolarimeter (Jasco). 20 mM SDS, 20 mM DDM, or 4 mM liposomes in NaPi buffer were mixed with 20 µM peptide in a volume of 200 µl and analyzed in a cuvette with 1 mm path length from 260–190 nm at 22°C. The parameters were as follows: standard sensitivity, 1 nm data pitch, digital integration time of 1 s, 1 nm bandwidth, 100 nm/min scanning speed, and three repeats for each measurement. Blank measurements without peptide were subtracted from the spectra before analysis. Values <200 nm were omitted from the final graph because of the exceeded high tension voltage (>700 V) of the detector. Mean residue ellipticity values were calculated using the formula

$$[\theta]mrw = \frac{MRW*\theta obs}{10*d*c} deg.*cm^{2}*dmol^{-1}$$

with *MRW* as mean residue weight, *d* as path length in centimeters, and *c* as peptide concentration in grams per milliliter.

Generation of MBP-Opi1 constructs for expression in *E. coli*

For the expression of the N-terminally tagged MBP-Opi1 fusion protein, MBP-Opi1^{R180*}, MBP-Opi1^{S114*}, and mutant variants of MBP-Opi1^{R180*}, we used the plasmid pMAL-OPI1 (Sreenivas and Carman, 2003) provided by G.M. Carman (Rutgers University, New Brunswick, NJ). The codons that were mutated and the corresponding primers are listed in Table S3. Site-directed mutagenesis was either conducted using a slightly modified QuikChange method (Agilent Technologies) with the PHUSION polymerase (New England Biolabs, Inc.) or using the Q5 site-directed mutagenesis kit (New England Biolabs, Inc.) indicated by a Q5 suffix in the primer names in Table S3.

Generation of Opi1-mGFP constructs and chromosomal integration in yeast

For the generation of Opi1-mGFP knock-in constructs, we used the pFA6a-mGFP-NatMX6 construct provided by K. Natter (University of Graz, Graz, Austria). First, we amplified a C-terminal *OPI1* homology region that is 3–556 bp downstream from the *OPI1* stop codon with overhangs for EcoRI and SpeI using the primers RE529 and RE530 to generate plasmid pFA6a-mGFP-NatMX6–C terminus homology by restriction-based cloning. For the generation of pFA6a-promoter-OPI1-mGFP-NatMX6–C terminus homology, we amplified the *OPI1* open reading frame including 275 bases upstream the start codon from genomic DNA with overhangs for the restriction enzymes HindIII and BamHI using the primers RE528 and RE440 and classical cloning. Site-directed mutagenesis was performed with primers listed in Table S3. After plasmid isolation and validation by DNA sequencing (SeqLab), 3 µg plasmid was digested with NotI (New England Biolabs, Inc.) to yield a linear DNA fragment containing the *OPI1* promoter, the open reading frame of *OPI1*, and a C-terminal homology region for transforming BY4742 or *scs2* yeast strains using the LiAc method. Transformants were selected on YPD plates containing 100 µg/ml nourseothricin, and positive clones were verified via DNA sequencing after colony PCR using the primers RE548 and RE916.

For the generation of Opi1-mRFP knock-in constructs, we used the pFA6a-mRFP-KanMX4 construct provided by K. Natter. The mRFP-KanMX4 cassette was amplified with overhangs for chromosomal insertion upstream of the stop codon of *OPI1* using the primers RE647 and RE648. The amplified fragment was purified using the PCR purification kit (QIAGEN), and 1 µg purified fragment was used for transformation of BY4741 using the LiAc method. Transformants were selected on YPD plates containing 100 µg/ml kanamycin, and the correct insertion of mRFP was validated by colony PCR using the primers RE649 and RE646. Diploid strains bearing Opi1-mGFP as one allele and native Opi1-mRFP as the other allele were generated by mating of the haploid strains followed by selection for diploid cells on YPD medium containing 100 µg/ml nourseothricin and 100 µg/ml kanamycin.

Expression and purification of recombinant MBP-Opi1 protein variants

The *E. coli* BL21-CodonPlus(DE3)-RIL strain (Agilent Technologies) was used for heterologous production of MBP-Opi1 variants. Cells were cultivated overnight at 37°C under constant agitation (at 220 rpm) in 5 ml lysogeny broth medium (1% peptone, 0.5% yeast extract, and 1% sodium chloride) containing 100 µg/ml ampicillin and 34 µg/ml chloramphenicol. The main culture was inoculated from this overnight culture to an OD_{600} of 0.25 in 250 ml fresh lysogeny broth ampicillin/chloramphenicol medium. At an OD_{600} of 0.5–0.6, heterologous gene expression was induced using 500 µM IPTG. Cells were harvested 3 h after induction. The cell pellets (400–500 OD_{600} units) were washed once in ice-cold protein purification (PP) buffer (50 mM Hepes, 150 mM NaCl, and 1 mM EDTA, pH 7.4) and stored at −20°C.

Cells were thawed on ice and resuspended in 22 ml ice-cold protein lysis buffer (50 mM Hepes, 150 mM NaCl, 1 mM EDTA, 2 mM DTT, 1 mM AEBSF, 10 µg/ml chymostatin, 10 µg/ml antipain, 10 µg/ml pepstatin, and 5 U/ml benzonase nuclease). Cell lysis was performed using a VS 70T sonotrode (20% amplitude; 0.7 s pulse and 0.3 s rest; 3× 30 s with 1 min cooling in between) on a Sonoplus HD 3100 (Bandelin). Cell debris was removed by centrifugation at 50,000 *g* for 30 min at 4°C. The supernatant was incubated with 2 ml washed amylose beads for 15 min at 4°C and under constant rocking and was then subjected to gravity flow affinity columns. Unbound protein was washed away using 40 ml PP buffer. The first elution with 1 ml protein elution buffer (PP buffer containing 10 mM maltose) was discarded. The affinity-purified protein was then eluted in 3 × 2 ml fractions. The protein concentration was determined by absorption spectroscopy using a NanoDrop 1000 spectrophotometer (PeqLab) at 280 nm with the protein-specific molecular weight, and the extinction coefficient was calculated by the ExPASy ProtParam tool. The purified proteins were mixed with 5× reducing protein sample buffer (8 M urea, 0.15% bromophenol blue, 5 mM EDTA, 10% SDS, 0.1 M Tris-HCl, pH 6.8, 4% glycerol, and 4% β-mercaptoethanol), boiled for 5 min at 95°C, and subjected to SDS-PAGE to check the quality of the purified proteins. For further preparation and analytic purposes, MBP-Opi1 variants were subjected to SEC using a Superdex 200 increase 10/300 GL on an ÄKTA pure system (GE Healthcare). 500 µg protein was injected using a 500-µl loop and a flow rate of 0.5 ml/min in PP buffer. The void volume of the column (V_0) was determined using Blue Dextran eluting at 8.9 ml.

LF assays

Liposomes and protein variants were mixed at a molar protein: lipid ratio of 1:3,300 in a total volume of 150 µl and incubated for 30 min at room temperature in an ultracentrifugation tube. For example, 80 µl liposomes (4 mM) in NaPi buffer and 6 µg protein in 70 µl PP buffer were mixed to yield 2.1 mM liposomes and 0.63 µM protein in 150 µl LF buffer (25 mM Hepes, 10 mM sodium phosphate, 150 mM sodium chloride, and 0.5 mM EDTA, pH 7.4). After incubation, 100 µl of 75% sucrose dissolved in LF buffer was added and gently mixed with the sample to yield a final concentration of 30% sucrose. 200 µl of 20% sucrose dissolved in LF buffer was carefully layered on top of the 30% sucrose fraction, and subsequently,

50 µl LF buffer was layered on top of the 20% sucrose fraction, yielding 500 µl of total volume. Sucrose density gradient centrifugation was conducted for 1 h at 22°C at a speed of 240,000 *g* in a TL-100 ultracentrifuge using a TLA 120.1 rotor (Beckman Coulter). Microlance 3 steel needles (BD) were used to collect four fractions of 125 µl from the bottom of the tube. Each fraction was mixed with 25 µl of 5× reducing protein sample buffer and boiled for 5 min at 95°C, and then 10 µl of each fraction was subjected to SDS-PAGE using gradient gels (4.5–15%; Bio-Rad Laboratories). Gels were stained with Instant Blue to visualize proteins as well as lipids. Protein amount of each fraction was quantified by densitometry using ImageJ (National Institutes of Health). The bound fraction was determined as the amount of protein in the top fraction divided by the total protein content in all fractions together.

Yeast viability assay and Opi⁻ test

Yeast strains were cultivated overnight in 3 ml YPD (1% yeast extract, 2% peptone, and 2% glucose) to an optical density (OD_{600}) of ∼10. Five OD_{600} units of cells were washed twice with sterile water and spotted onto the respective plates using a metal stamp with a 1:10 dilution series starting with an OD_{600} of 1. Plates were scanned after 2 d growth on solid synthetic complete dextrose (SCD) medium containing 75 µM inositol (+Ino) or lacking inositol (–Ino) at 30°C or 37°C.

For the Opi⁻ test, yeast strains were cultivated and washed with sterile water. 5 µl with an OD_{600} of 1 were spotted onto SCD plates lacking inositol. After 1 d incubation at 30°C, an inositol auxotrophic tester strain (AID strain; provided by S.A. Henry, Cornell University, Ithaca, USA; washed and dissolved in sterile water) was sprayed on the plate, followed by incubation for additional 2 d at 30°C. Overproduction and secretion of inositol (Opi⁻ phenotype) was apparent from a red halo from the tester strain around the spotted yeast strains.

Cell cultivation and calculation of growth rate

Yeast strains were cultivated overnight in 3 ml SCD +Ino medium to reach an OD_{600} of ∼7. A fresh culture was inoculated with the overnight culture to an OD_{600} of 0.33 in 3 ml SCD +Ino medium and cultivated for 4.5 h. Cells were then harvested by centrifugation (4,200 rpm for 3 min at 24°C), washed once with prewarmed SCD –Ino, and rediluted in 3 ml fresh and prewarmed SCD –Ino medium for further cultivation at 30°C under constant agitation at 220 rpm. The OD_{600} was measured every 45 min up to 6.75 h, and the growth rate was calculated from the time window between 3 and 6 h after the medium shift to guarantee inositol-depleted conditions for all strains (Gaspar et al., 2011; Hofbauer et al., 2014).

Fluorescence microscopy and image quantification

Cells were grown as described in the above section. Microscopic images were recorded after 2 h inositol depletion on an LSM770 confocal laser scanning microscope (ZEISS) with spectral detection and a Plan Apochromat 63× 1.40 NA oil differential interference contrast M27 objective. GFP fluorescence was excited at 488 nm and detected between 493–586 nm. RFP fluorescence was excited at 561 nm and detected between 578–696 nm. For better image visualization, the contrast was adjusted equally for all images using ZEN 2 lite software (ZEISS) with no further processing.

For quantification, the raw images were smoothed with a Gaussian filter of radius 2. To extract the nucleus-related structures, either nuclear localization or nuclear ER localization, the objects with highest intensities were identified by an intensity clustering algorithm. All objects above a size threshold were classified as nucleus-related structures. The size threshold was manually adjusted for the different conditions and ranged between 0.73 and 2.15 μm^2. For each nucleus-related structure, the localization index $\frac{d}{r}$ was calculated, where d is the maximum distance of the pixels of an object to the centroid of the object, and r is the equivalent disk radius, which in this case was particularly the radius of a disk consisting of the same number of pixels as the object of interest. If the fluorescent particles had a nuclear localization, the observed shape was a blob with the size of the nucleus. The equivalent disk radius r of a blob was comparable with d, and the localization index was close to one. If the fluorescent particles localized to the ER, one observed a ring-shaped structure around the nucleus. For a ring, the maximum distance to the centroid was bigger than the radius of an area-equivalent disk ($r < d$), and the localization index was large. We set the threshold between blob and ring to 1.3. Hence, a localization index of ≤1.3 indicated nuclear localization. For a localization index >1.3, we had localization to the nuclear ER. For each condition, we analyzed at least 190 cells in four images. The image analysis was implemented in Mathematica 11.1 (Wolfram Research). The code and an example calculation are available at https://www.physikalischebiologie.de/downloads.

Analysis of Opi1-mGFP protein levels using immunoblotting

Cells were grown as described in the Cell cultivation and calculation of growth rate section. 2 h after the shift to medium lacking inositol, three OD_{600} units were harvested (3,500 rpm for 5 min at 4°C) and washed once with ice-cold water. Cell pellets were resuspended in 400 µl 12.5% TCA and stored at –20°C over night. TCA was removed by centrifugation at 13,000 rpm for 5 min at room temperature, and the cell pellets were washed with 500 µl 80% ice-cold acetone, air-dried for 2 min, and dissolved in 160 µl of a mixture of 1% SDS and 0.1 N NaOH. 40 µl of 5× protein sample buffer was added, and samples were boiled at 95°C for 5 min. SDS-PAGE was performed using 7.5% gel (Bio-Rad Laboratories), and proteins were blotted onto nitrocellulose membranes (Roth) and incubated with 5% skim milk powder (Fluka) in TBST (50 mM Tris, 150 mM sodium chloride, pH 8.0, and 0.1% Tween-20) for 30 min to reduce unspecific antibody binding. Blots were then decorated with 2.5% skim milk powder in TBST containing either mouse anti-GFP antibody (1:1,000; 11-814-460-001; Roche) or mouse anti-Pgk1 antibody (1:20,000; 22C5D8; Thermo Fisher Scientific) as primary antibodies and anti–mouse HRP antibody (1:20,000; 115-035-003; Dianova) as secondary antibody for detection with SuperSignal West Femto maximum-sensitivity substrate (Thermo Fisher Scientific) using the ChemiDoc MP imaging system (Bio-Rad Laboratories).

CG MD simulations

We modeled a 22-mer peptide (QKLSRAIAKGKDNLKEYKLNMS) into an α-helical conformation using the UCSF CHIMERA

software package (Pettersen et al., 2004). In a CG representation using in the MARTINI force field (Marrink et al., 2007; de Jong et al., 2013), the helix was placed in a cubic box of 10 × 10 × 10 nm^3 containing water, a lipid bilayer, and 150 mM sodium chloride assembled using the insane tool (Wassenaar et al., 2015). The helix was placed at a distance of 4 nm from the bilayer's center of mass. We set up different bilayer systems with different lipid compositions, all spanning the x–y plane. The bilayer system designated as 20% PA was composed of 60 mol% POPC, 20 mol% DOPC, and 20 mol% DOPA. The bilayer designated as 20% PS was composed of 60 mol% POPC, 20 mol% DOPC, and 20 mol% DOPS. The bilayer designated as 20% PA/PS contained 60 mol% POPC, 20 mol% DOPA, and 20 mol% DOPS. Acyl chains were kept constant with a ratio of 6:4 (PO/DO), whereas the head group species and their relative ratios were varied. Each system was simulated for 1 µs.

CG simulations were performed using the GROMACS software package (version 5.1.3; Abraham et al., 2015) with the MARTINI force field version 2.2. The integration time step was set to 20 fs with a neighbor list update every 20 steps. Nonbonded interactions were cut off at 1.1 nm using the Verlet algorithm. Temperature was kept constant at 310 K using the Velocity Rescale (Bussi et al., 2007) thermostat with a characteristic time of 1 ps. A pressure of 1 bar was maintained by semiisotropic pressure coupling using the Parrinello-Rahman algorithm and a characteristic time of 12 ps (Parrinello and Rahman, 1980). Periodic boundary conditions were imposed.

Backmapping of CG systems to an atomistic representation

We used CHARMM-GUI (Jo et al., 2007, 2008, 2009, 2014; Wassenaar et al., 2014; Lee et al., 2016) to lift all three CG systems to an atomistic description in the CHARMM36 force field (Klauda et al., 2010; Vanommeslaeghe et al., 2010; Best et al., 2014). 150 mM NaCl and neutralizing counterions were added. The energy of the system was minimized for 5,000 steps, keeping a restraint on all heavy atoms. Constant-volume ensemble equilibration was run for 50 ns at a temperature at 310 K using a time step of 1 fs. Subsequently, a constant-pressure ensemble equilibration was run for 375 ns with a time step of 2 fs to stabilize the pressure at 1 bar. Both the Berendsen barostat and thermostat were used during equilibration (Berendsen et al., 1984). Nonbonded interactions were cut off at 1.2 nm. During the production simulations, we used a Velocity Rescale thermostat (Bussi et al., 2007) at 310 K and the Parrinello-Rahman barostat (Parrinello and Rahman, 1980) with semiisotropic pressure coupling, applying them on the protein, membrane, and solvent with characteristic times of 1 and 5 ps, respectively. We simulated the systems for 10 µs each for the WT AH and for 2.4 µs for the mutant 5K5R AH.

Analysis of lipid localization

For every frame in the trajectory, we binned phosphate atoms belonging to a specific lipid type according to their x and y positions on a 2D grid using a bin area of 1 $Å^2$ and sampling every 500 ps. We then obtained a 2D in-plane rotation angle for every frame by using an in-plane least-square fit of the backbone C_α atoms to a reference structure of the AH aligned along the x axis. For every frame, the 2D grid was interpolated by a third order spline and rotated by the calculated angle about the direction orthogonal to the plane of the membrane. By considering periodic boundary conditions, the grid in every frame was extended and cropped after the rotation to keep the original dimensions. Finally, we calculated the lipid density by averaging all 2D grids the entire trajectory except for the first 100 ns.

Calculation of distance distributions

We centered the AH at the origin and aligned the AH on the x axis with the N terminus pointing in the positive x direction. We then calculated the pairwise distances from a reference point to all lipids localized in a given area. We defined the combined C_α center of mass of three amino acids (K112, R115, and K119 for the KRK motif; K121, K125, and K128 for the 3K motif) as our reference points p_{KRK} and p_{3K}. We then defined two boundaries $p_x \pm 10$ Å on the x axis from each point of reference. For p_{3K}, we considered lipids between the boundaries with negative y values, and for p_{KRK}, we considered lipids with positive y values. We then calculated for every frame the 2D Euclidean distance to all lipids contained in the squared area adjacent to the points of interest. We binned all calculated distances into 200 bins using a bin width of 0.1 Å, sampling every 500 ps.

Residence times

We calculated for each trajectory the residence time of lipids in the neighborhood of residues K112, R115, and K119, or K121, K125, and K128. We removed the coordinates of the center of mass of all atoms and aligned the AH onto the x axis as described above. We defined three rectangular areas A_b, A_i, and A_u around the region of interest p, and in each frame, we assigned a state S to each lipid based on its localization in a given area: S_b (bound), S_i (intermediate), or S_u (unbound). We considered a lipid to be bound when first entering region A_b and to dissociate when first hitting region A_u. We also defined an intermediate region A_i in which the lipids commit for association or disassociation. We calculated the residence time by summation of the total time spent in state S_b and S_i before hitting state S_u again (Buchete and Hummer, 2008).

Trajectory analysis

We used VMD (Humphrey et al., 1996), GROMACS (Abraham et al., 2015), MDAnalysis (Michaud-Agrawal et al., 2011; Gowers et al., 2016), NumPy (van der Walt et al., 2011), SciPy (Jones et al., 2001), IPython (Pérez and Granger, 2007), and Matplotlib (Hunter, 2007) for the analysis and visualization of trajectories.

Online supplemental material

Fig. S1 shows amphipathic helices of proteins sensing PA-rich membranes. Fig. S2 shows quality controls of purified MBP-$Opi1^{R180*}$ variants and liposomes. Fig. S3 shows that Opi1 point mutations do not impair nuclear ER membrane binding of native Opi1 in diploid yeast cells. Fig. S4 shows details from MD simulations with the AH derived from WT Opi1. Fig. S5 provides additional in vivo and MD simulation data related to the 5K5R variant of Opi1. *E. coli and S. cerevisiae* strains used in this study are listed in Table S1, plasmids are listed in Table S2, and primers are listed in Table S3.

Acknowledgments

We acknowledge George M. Carman and Klaus Natter for kindly providing crucial reagents. The AID strain was kindly provided by Susan A. Henry. We thank Sepp D. Kohlwein for critically reading the manuscript. H.F. Hofbauer and R. Ernst acknowledge Christoph Bock and Toni Radanović for their technical support as well as Stefano Vanni (Université de Fribourg, Fribourg, Switzerland) for suggesting the MD simulation with a mixed bilayer. M. Gecht, R. Covino, and G. Hummer acknowledge discussions with Drs. Lukas Stelzl, Ahmadreza Mehdipour, and Max Linke.

H.F. Hofbauer is funded by the Erwin Schrödinger fellowship of the Austrian Science Fund (FWF): J3987-B21. The work was supported by the Deutsche Forschungsgemeinschaft (EN608/2-1 to R. Ernst; SFB807 Transport and Communication across Biological Membranes to R. Ernst and G. Hummer; CEF-MC II to E.H.K. Stelzer and R. Ernst; and EC-115 to E.H.K. Stelzer). M. Gecht, R. Covino, and G. Hummer acknowledge support from the Max Planck Society.

The authors declare no competing financial interests.

Author contributions: R. Ernst supervised the project. H.F. Hofbauer, M. Gecht, R. Covino, and R. Ernst conceived the experimental design. H.F. Hofbauer and R. Ernst wrote the manuscript. H.F. Hofbauer performed the experimental work. M. Gecht, R. Covino, and G. Hummer designed and conducted MD simulations and analyzed the data. S.C. Fischer and E.H.K. Stelzer supported quantitative live-cell microscopy. A. Seybert and A.S. Frangakis performed cryoelectron-microscopic imaging of liposomes.

Submitted: 5 February 2018
Revised: 28 May 2018
Accepted: 18 June 2018

References

Abraham, M.J., T. Murtola, R. Schulz, S. Páll, J.C. Smith, B. Hess, and E. Lindah. 2015. Gromacs: High performance molecular simulations through multi-level parallelism from laptops to supercomputers. *SoftwareX*. 1–2:19–25. https://doi.org/10.1016/j.softx.2015.06.001

Antonny, B. 2011. Mechanisms of membrane curvature sensing. *Annu. Rev. Biochem.* 80:101–123. https://doi.org/10.1146/annurev-biochem-052809-155121

Antonny, B., S. Vanni, H. Shindou, and T. Ferreira. 2015. From zero to six double bonds: phospholipid unsaturation and organelle function. *Trends Cell Biol.* 25:427–436. https://doi.org/10.1016/j.tcb.2015.03.004

Athenstaedt, K., and G. Daum. 1999. Phosphatidic acid, a key intermediate in lipid metabolism. *Eur. J. Biochem.* 266:1–16. https://doi.org/10.1046/j.1432-1327.1999.00822.x

Ballweg, S., and R. Ernst. 2017. Control of membrane fluidity: the OLE pathway in focus. *Biol. Chem.* 398:215–228. https://doi.org/10.1515/hsz-2016-0277

Berendsen, H.J.C., J.P.M. Postma, W.F. Van Gunsteren, A. Dinola, and J.R. Haak. 1984. Molecular dynamics with coupling to an external bath. *J. Chem. Phys.* 81:3684–3690. https://doi.org/10.1063/1.448118

Best, R.B., W. Zheng, and J. Mittal. 2014. Balanced protein-water interactions improve properties of disordered proteins and non-specific protein association. *J. Chem. Theory Comput.* 10:5113–5124. https://doi.org/10.1021/ct500569b

Bigay, J., and B. Antonny. 2012. Curvature, lipid packing, and electrostatics of membrane organelles: defining cellular territories in determining specificity. *Dev. Cell.* 23:886–895. https://doi.org/10.1016/j.devcel.2012.10.009

Buchete, N.V., and G. Hummer. 2008. Coarse master equations for peptide folding dynamics. *J. Phys. Chem. B.* 112:6057–6069. https://doi.org/10.1021/jp0761665

Bussi, G., D. Donadio, and M. Parrinello. 2007. Canonical sampling through velocity rescaling. *J. Chem. Phys.* 126:014101. https://doi.org/10.1063/1.2408420

Clark, A.L., and F. Urano. 2016. Endoplasmic reticulum stress in beta cells and autoimmune diabetes. *Curr. Opin. Immunol.* 43:60–66. https://doi.org/10.1016/j.coi.2016.09.006

Covino, R., S. Ballweg, C. Stordeur, J.B. Michaelis, K. Puth, F. Wernig, A. Bahrami, A.M. Ernst, G. Hummer, and R. Ernst. 2016. A eukaryotic sensor for membrane lipid saturation. *Mol. Cell.* 63:49–59. https://doi.org/10.1016/j.molcel.2016.05.015

Cunha, D.A., P. Hekerman, L. Ladrière, A. Bazarra-Castro, F. Ortis, M.C. Wakeham, F. Moore, J. Rasschaert, A.K. Cardozo, E. Bellomo, et al. 2008. Initiation and execution of lipotoxic ER stress in pancreatic beta-cells. *J. Cell Sci.* 121:2308–2318. https://doi.org/10.1242/jcs.026062

Deguil, J., L. Pineau, E.C. Rowland Snyder, S. Dupont, L. Beney, A. Gil, G. Frapper, and T. Ferreira. 2011. Modulation of lipid-induced ER stress by fatty acid shape. *Traffic.* 12:349–362. https://doi.org/10.1111/j.1600-0854.2010.01150.x

de Jong, D.H., G. Singh, W.F.D. Bennett, C. Arnarez, T.A. Wassenaar, L.V. Schäfer, X. Periole, D.P. Tieleman, and S.J. Marrink. 2013. Improved parameters for the martini coarse-grained protein force field. *J. Chem. Theory Comput.* 9:687–697. https://doi.org/10.1021/ct300646g

de Kroon, A.I.P.M., P.J. Rijken, and C.H. De Smet. 2013. Checks and balances in membrane phospholipid class and acyl chain homeostasis, the yeast perspective. *Prog. Lipid Res.* 52:374–394. https://doi.org/10.1016/j.plipres.2013.04.006

Drin, G., and B. Antonny. 2010. Amphipathic helices and membrane curvature. *FEBS Lett.* 584:1840–1847. https://doi.org/10.1016/j.febslet.2009.10.022

Ejsing, C.S., J.L. Sampaio, V. Surendranath, E. Duchoslav, K. Ekroos, R.W. Klemm, K. Simons, and A. Shevchenko. 2009. Global analysis of the yeast lipidome by quantitative shotgun mass spectrometry. *Proc. Natl. Acad. Sci. USA.* 106:2136–2141. https://doi.org/10.1073/pnas.0811700106

Ernst, R., C.S. Ejsing, and B. Antonny. 2016. Homeoviscous adaptation and the regulation of membrane lipids. *J. Mol. Biol.* 428(24, 24 Pt A):4776–4791. https://doi.org/10.1016/j.jmb.2016.08.013

Ernst, R., S. Ballweg, and I. Levental. 2018. Cellular mechanisms of physicochemical membrane homeostasis. *Curr. Opin. Cell Biol.* 53:44–51. https://doi.org/10.1016/j.ceb.2018.04.013

Findlay, B., G.G. Zhanel, and F. Schweizer. 2010. Cationic amphiphiles, a new generation of antimicrobials inspired by the natural antimicrobial peptide scaffold. *Antimicrob. Agents Chemother.* 54:4049–4058. https://doi.org/10.1128/AAC.00530-10

Foster, D.A. 2009. Phosphatidic acid signaling to mTOR: signals for the survival of human cancer cells. *Biochim. Biophys. Acta.* 1791:949–955. https://doi.org/10.1016/j.bbalip.2009.02.009

Frank, C., H. Keilhack, F. Opitz, O. Zschörnig, and F.D. Böhmer. 1999. Binding of phosphatidic acid to the protein-tyrosine phosphatase SHP-1 as a basis for activity modulation. *Biochemistry.* 38:11993–12002. https://doi.org/10.1021/bi982586w

Ganesan, S., B.N. Shabits, and V. Zaremberg. 2016. Tracking diacylglycerol and phosphatidic acid pools in budding yeast. *Lipid Insights.* 8(Suppl 1):75–85. https://doi.org/10.4137/Lpi.s31781

Gaspar, M.L., H.F. Hofbauer, S.D. Kohlwein, and S.A. Henry. 2011. Coordination of storage lipid synthesis and membrane biogenesis: evidence for cross-talk between triacylglycerol metabolism and phosphatidylinositol synthesis. *J. Biol. Chem.* 286:1696–1708. https://doi.org/10.1074/jbc.M110.172296

Gaspar, M.L., Y.F. Chang, S.A. Jesch, M. Aregullin, and S.A. Henry. 2017. Interaction between repressor Opi1p and ER membrane protein Scs2p facilitates transit of phosphatidic acid from the ER to mitochondria and is essential for *INO1* gene expression in the presence of choline. *J. Biol. Chem.* 292:18713–18728. https://doi.org/10.1074/jbc.M117.809970

Gautier, R., D. Douguet, B. Antonny, and G. Drin. 2008. HELIQUEST: a web server to screen sequences with specific α-helical properties. *Bioinformatics.* 24:2101–2102. https://doi.org/10.1093/bioinformatics/btn392

Gerl, M.J., J.L. Sampaio, S. Urban, L. Kalvodova, J.M. Verbavatz, B. Binnington, D. Lindemann, C.A. Lingwood, A. Shevchenko, C. Schroeder, and K. Simons. 2012. Quantitative analysis of the lipidomes of the influenza virus envelope and MDCK cell apical membrane. *J. Cell Biol.* 196:213–221. https://doi.org/10.1083/jcb.201108175

Ghaemmaghami, S., W.K. Huh, K. Bower, R.W. Howson, A. Belle, N. Dephoure, E.K. O'Shea, and J.S. Weissman. 2003. Global analysis of protein expression in yeast. *Nature.* 425:737–741. https://doi.org/10.1038/nature02046

Goldstein, J.L., R.A. DeBose-Boyd, and M.S. Brown. 2006. Protein sensors for membrane sterols. *Cell.* 124:35–46. https://doi.org/10.1016/j.cell.2005.12.022

Gowers, R.J., M. Linke, J. Barnoud, T.J.E. Reddy, M.N. Melo, S.L. Seyler, J. Domański, D.L. Dotson, S. Buchoux, I.M. Kenney, and O. Beckstein. 2016. MDAnalysis: A Python Package for the Rapid Analysis of Molecular Dynamics Simulations. *Proc. 15th Python Sci. Conf.* 98–105.

Graves, J.A., and S.A. Henry. 2000. Regulation of the yeast INO1 gene. The products of the INO2, INO4 and OPI1 regulatory genes are not required for repression in response to inositol. *Genetics.* 154:1485–1495.

Greenberg, M.L., B. Reiner, and S.A. Henry. 1982. Regulatory mutations of inositol biosynthesis in yeast: isolation of inositol-excreting mutants. *Genetics.* 100:19–33.

Grippa, A., L. Buxó, G. Mora, C. Funaya, F.Z. Idrissi, F. Mancuso, R. Gomez, J. Muntanyà, E. Sabidó, and P. Carvalho. 2015. The seipin complex Fld1/Ldb16 stabilizes ER-lipid droplet contact sites. *J. Cell Biol.* 211:829–844. https://doi.org/10.1083/jcb.201502070

Halbleib, K., K. Pesek, R. Covino, H.F. Hofbauer, D. Wunnicke, I. Hänelt, G. Hummer, and R. Ernst. 2017. Activation of the Unfolded Protein Response by Lipid Bilayer Stress. *Mol. Cell.* 67:673–684. https://doi.org/10.1016/j.molcel.2017.06.012

Henry, S.A., S.D. Kohlwein, and G.M. Carman. 2012. Metabolism and regulation of glycerolipids in the yeast Saccharomyces cerevisiae. *Genetics.* 190:317–349. https://doi.org/10.1534/genetics.111.130286

Hofbauer, H.F., F.H. Schopf, H. Schleifer, O.L. Knittelfelder, B. Pieber, G.N. Rechberger, H. Wolinski, M.L. Gaspar, C.O. Kappe, J. Stadlmann, et al. 2014. Regulation of gene expression through a transcriptional repressor that senses acyl-chain length in membrane phospholipids. *Dev. Cell.* 29:729–739. https://doi.org/10.1016/j.devcel.2014.04.025

Holthuis, J.C.M., and A.K. Menon. 2014. Lipid landscapes and pipelines in membrane homeostasis. *Nature.* 510:48–57. https://doi.org/10.1038/nature13474

Horchani, H., M. de Saint-Jean, H. Barelli, and B. Antonny. 2014. Interaction of the Spo20 membrane-sensor motif with phosphatidic acid and other anionic lipids, and influence of the membrane environment. *PLoS One.* 9:e113484. https://doi.org/10.1371/journal.pone.0113484

Humphrey, W., A. Dalke, and K. Schulten. 1996. VMD: visual molecular dynamics. *J. Mol. Graph.* 14:33–38. https://doi.org/10.1016/0263-7855(96)00018-5

Hunter, J.D. 2007. Matplotlib: A 2D graphics environment. *Comput. Sci. Eng.* 9:90–95. https://doi.org/10.1109/MCSE.2007.55

Jacquemyn, J., A. Cascalho, and R.E. Goodchild. 2017. The ins and outs of endoplasmic reticulum-controlled lipid biosynthesis. *EMBO Rep.* 18:1905–1921. https://doi.org/10.15252/embr.201643426

Jesch, S.A., X. Zhao, M.T. Wells, and S.A. Henry. 2005. Genome-wide analysis reveals inositol, not choline, as the major effector of Ino2p-Ino4p and unfolded protein response target gene expression in yeast. *J. Biol. Chem.* 280:9106–9118. https://doi.org/10.1074/jbc.M411770200

Jin, L., X. Bai, N. Luan, H. Yao, Z. Zhang, W. Liu, Y. Chen, X. Yan, M. Rong, R. Lai, and Q. Lu. 2016. A Designed Tryptophan- and Lysine/Arginine-Rich Antimicrobial Peptide with Therapeutic Potential for Clinical Antibiotic-Resistant Candida albicans Vaginitis. *J. Med. Chem.* 59:1791–1799. https://doi.org/10.1021/acs.jmedchem.5b01264

Jo, S., T. Kim, and W. Im. 2007. Automated builder and database of protein/membrane complexes for molecular dynamics simulations. *PLoS One.* 2:e880. https://doi.org/10.1371/journal.pone.0000880

Jo, S., T. Kim, V.G. Iyer, and W. Im. 2008. CHARMM-GUI: a web-based graphical user interface for CHARMM. *J. Comput. Chem.* 29:1859–1865. https://doi.org/10.1002/jcc.20945

Jo, S., J.B. Lim, J.B. Klauda, and W. Im. 2009. CHARMM-GUI Membrane Builder for mixed bilayers and its application to yeast membranes. *Biophys. J.* 97:50–58. https://doi.org/10.1016/j.bpj.2009.04.013

Jo, S., X. Cheng, S.M. Islam, L. Huang, H. Rui, A. Zhu, H.S. Lee, Y. Qi, W. Han, K. Vanommeslaeghe, et al. 2014. CHARMM-GUI PDB manipulator for advanced modeling and simulations of proteins containing nonstandard residues. *Adv. Protein Chem. Struct. Biol.* 96:235–265. https://doi.org/10.1016/bs.apcsb.2014.06.002

Jones, E., E. Oliphant, P. Peterson, et al. SciPy: Open Source Scientific Tools for Python, 2001-, http://www.scipy.org/ [Online; accessed 2018-06-19].

Kaiser, H.J., M.A. Surma, F. Mayer, I. Levental, M. Grzybek, R.W. Klemm, S. Da Cruz, C. Meisinger, V. Müller, K. Simons, and D. Lingwood. 2011. Molecular convergence of bacterial and eukaryotic surface order. *J. Biol. Chem.* 286:40631–40637. https://doi.org/10.1074/jbc.M111.276444

Karanasios, E., G.-S. Han, Z. Xu, G.M. Carman, and S. Siniossoglou. 2010. A phosphorylation-regulated amphipathic helix controls the membrane translocation and function of the yeast phosphatidate phosphatase. *Proc. Natl. Acad. Sci. USA.* 107:17539–17544. https://doi.org/10.1073/pnas.1007974107

Kassas, N., P. Tryoen-Tóth, M. Corrotte, T. Thahouly, M.F. Bader, N.J. Grant, and N. Vitale. 2012. Genetically encoded probes for phosphatidic acid. *Methods Cell Biol.* 108:445–459. https://doi.org/10.1016/B978-0-12-386487-1.00020-1

Kassas, N., E. Tanguy, T. Thahouly, L. Fouillen, D. Heintz, S. Chasserot-Golaz, M.F. Bader, N.J. Grant, and N. Vitale. 2017. Comparative characterization of phosphatidic acid sensors and their localization during frustrated phagocytosis. *J. Biol. Chem.* 292:4266–4279. https://doi.org/10.1074/jbc.M116.742346

Kitai, Y., H. Ariyama, N. Kono, D. Oikawa, T. Iwawaki, and H. Arai. 2013. Membrane lipid saturation activates IRE1α without inducing clustering. *Genes Cells.* 18:798–809. https://doi.org/10.1111/gtc.12074

Klauda, J.B., R.M. Venable, J.A. Freites, J.W. O'Connor, D.J. Tobias, C. Mondragon-Ramirez, I. Vorobyov, A.D. MacKerell Jr., and R.W. Pastor. 2010. Update of the CHARMM all-atom additive force field for lipids: validation on six lipid types. *J. Phys. Chem. B.* 114:7830–7843. https://doi.org/10.1021/jp101759q

Klemm, R.W., C.S. Ejsing, M.A. Surma, H.J. Kaiser, M.J. Gerl, J.L. Sampaio, Q. de Robillard, C. Ferguson, T.J. Proszynski, A. Shevchenko, and K. Simons. 2009. Segregation of sphingolipids and sterols during formation of secretory vesicles at the trans-Golgi network. *J. Cell Biol.* 185:601–612. https://doi.org/10.1083/jcb.200901145

Klose, C., M.A. Surma, M.J. Gerl, F. Meyenhofer, A. Shevchenko, and K. Simons. 2012. Flexibility of a eukaryotic lipidome--insights from yeast lipidomics. *PLoS One.* 7:e35063. https://doi.org/10.1371/journal.pone.0035063

Kooijman, E.E., K.M. Carter, E.G. van Laar, V. Chupin, K.N.J. Burger, and B. de Kruijff. 2005. What makes the bioactive lipids phosphatidic acid and lysophosphatidic acid so special? *Biochemistry.* 44:17007–17015. https://doi.org/10.1021/bi0518794

Ladokhin, A.S., and S.H. White. 1999. Folding of amphipathic α-helices on membranes: energetics of helix formation by melittin. *J. Mol. Biol.* 285:1363–1369. https://doi.org/10.1006/jmbi.1998.2346

Laplante, M., and D.M. Sabatini. 2012. mTOR signaling in growth control and disease. *Cell.* 149:274–293. https://doi.org/10.1016/j.cell.2012.03.017

Lee, J., X. Cheng, J.M. Swails, M.S. Yeom, P.K. Eastman, J.A. Lemkul, S. Wei, J. Buckner, J.C. Jeong, Y. Qi, et al. 2016. CHARMM-GUI Input Generator for NAMD, GROMACS, AMBER, OpenMM, and CHARMM/OpenMM Simulations Using the CHARMM36 Additive Force Field. *J. Chem. Theory Comput.* 12:405–413. https://doi.org/10.1021/acs.jctc.5b00935

Li, L., I. Vorobyov, and T.W. Allen. 2013. The different interactions of lysine and arginine side chains with lipid membranes. *J. Phys. Chem. B.* 117:11906–11920. https://doi.org/10.1021/jp405418y

Liu, X., R. Cao, S. Wang, J. Jia, and H. Fei. 2016. Amphipathicity Determines Different Cytotoxic Mechanisms of Lysine- or Arginine-Rich Cationic Hydrophobic Peptides in Cancer Cells. *J. Med. Chem.* 59:5238–5247. https://doi.org/10.1021/acs.jmedchem.5b02016

Liu, Y., Y. Su, and X. Wang. 2013. Phosphatidic acid-mediated signaling. *Adv. Exp. Med. Biol.* 991:159–176. https://doi.org/10.1007/978-94-007-6331-9_9

Loewen, C.J.R., and T.P. Levine. 2005. A highly conserved binding site in vesicle-associated membrane protein-associated protein (VAP) for the FFAT motif of lipid-binding proteins. *J. Biol. Chem.* 280:14097–14104. https://doi.org/10.1074/jbc.M500147200

Loewen, C.J.R., A. Roy, and T.P. Levine. 2003. A conserved ER targeting motif in three families of lipid binding proteins and in Opi1p binds VAP. *EMBO J.* 22:2025–2035. https://doi.org/10.1093/emboj/cdg201

Loewen, C.J.R., M.L. Gaspar, S.A. Jesch, C. Delon, N.T. Ktistakis, S.A. Henry, and T.P. Levine. 2004. Phospholipid metabolism regulated by a transcription factor sensing phosphatidic acid. *Science.* 304:1644–1647. https://doi.org/10.1126/science.1096083

Magdeleine, M., R. Gautier, P. Gounon, H. Barelli, S. Vanni, and B. Antonny. 2016. A filter at the entrance of the Golgi that selects vesicles according to size and bulk lipid composition. *eLife.* 5:e16988. https://doi.org/10.7554/eLife.16988

Marrink, S.J., H.J. Risselada, S. Yefimov, D.P. Tieleman, and A.H. de Vries. 2007. The MARTINI force field: coarse grained model for biomolecular simulations. *J. Phys. Chem. B.* 111:7812–7824. https://doi.org/10.1021/jp071097f

Michaud-Agrawal, N., E.J. Denning, T.B. Woolf, and O. Beckstein. 2011. MDAnalysis: a toolkit for the analysis of molecular dynamics simulations. *J. Comput. Chem.* 32:2319–2327. https://doi.org/10.1002/jcc.21787

Monné, M., M. Hermansson, and G. von Heijne. 1999. A turn propensity scale for transmembrane helices. *J. Mol. Biol.* 288:141–145. https://doi.org/10.1006/jmbi.1999.2657

Nakanishi, H., P. de los Santos, and A.M. Neiman. 2004. Positive and negative regulation of a SNARE protein by control of intracellular localization. *Mol. Biol. Cell.* 15:1802–1815. https://doi.org/10.1091/mbc.e03-11-0798

Odorizzi, G., M. Babst, and S.D. Emr. 2000. Phosphoinositide signaling and the regulation of membrane trafficking in yeast. *Trends Biochem. Sci.* 25:229–235. https://doi.org/10.1016/S0968-0004(00)01543-7

Öjemalm, K., T. Higuchi, P. Lara, E. Lindahl, H. Suga, and G. von Heijne. 2016. Energetics of side-chain snorkeling in transmembrane helices probed by nonproteinogenic amino acids. *Proc. Natl. Acad. Sci. USA.* 113:10559–10564. https://doi.org/10.1073/pnas.1606776113

Parrinello, M., and A. Rahman. 1980. Crystal structure and pair potentials: A molecular-dynamics study. *Phys. Rev. Lett.* 45:1196–1199. https://doi.org/10.1103/PhysRevLett.45.1196

Pérez, F., and B.E. Granger. 2007. IPython: A system for interactive scientific computing. *Comput. Sci. Eng.* 9:21–29. https://doi.org/10.1109/MCSE.2007.53

Pettersen, E.F., T.D. Goddard, C.C. Huang, G.S. Couch, D.M. Greenblatt, E.C. Meng, and T.E. Ferrin. 2004. UCSF Chimera--a visualization system for exploratory research and analysis. *J. Comput. Chem.* 25:1605–1612. https://doi.org/10.1002/jcc.20084

Pineau, L., J. Colas, S. Dupont, L. Beney, P. Fleurat-Lessard, J.M. Berjeaud, T. Bergès, and T. Ferreira. 2009. Lipid-induced ER stress: synergistic effects of sterols and saturated fatty acids. *Traffic.* 10:673–690. https://doi.org/10.1111/j.1600-0854.2009.00903.x

Puth, K., H.F. Hofbauer, J.P. Sáenz, and R. Ernst. 2015. Homeostatic control of biological membranes by dedicated lipid and membrane packing sensors. *Biol. Chem.* 396:1043–1058. https://doi.org/10.1515/hsz-2015-0130

Putta, P., J. Rankenberg, R.A. Korver, R. van Wijk, T. Munnik, C. Testerink, and E.E. Kooijman. 2016. Phosphatidic acid binding proteins display differential binding as a function of membrane curvature stress and chemical properties. *Biochim. Biophys. Acta.* 1858:2709–2716. https://doi.org/10.1016/j.bbamem.2016.07.014

Radanović, T., J. Reinhard, S. Ballweg, K. Pesek, and R. Ernst. 2018. An emerging group of membrane property sensors controls the physical state of organellar membranes to maintain their identity. *BioEssays.* 40:1700250. https://doi.org/10.1002/bies.201700250

Schneiter, R., and S.D. Kohlwein. 1997. Organelle structure, function, and inheritance in yeast: a role for fatty acid synthesis? *Cell.* 88:431–434. https://doi.org/10.1016/S0092-8674(00)81882-6

Schuck, S., W.A. Prinz, K.S. Thorn, C. Voss, and P. Walter. 2009. Membrane expansion alleviates endoplasmic reticulum stress independently of the unfolded protein response. *J. Cell Biol.* 187:525–536. https://doi.org/10.1083/jcb.200907074

Schüller, H.J., K. Richter, B. Hoffmann, R. Ebbert, and E. Schweizer. 1995. DNA binding site of the yeast heteromeric Ino2p/Ino4p basic helix-loop-helix transcription factor: structural requirements as defined by saturation mutagenesis. *FEBS Lett.* 370:149–152. https://doi.org/10.1016/0014-5793(95)00818-T

Shai, Y. 1999. Mechanism of the binding, insertion and destabilization of phospholipid bilayer membranes by α-helical antimicrobial and cell non-selective membrane-lytic peptides. *Biochim. Biophys. Acta.* 1462:55–70. https://doi.org/10.1016/S0005-2736(99)00200-X

Sreenivas, A., and G.M. Carman. 2003. Phosphorylation of the yeast phospholipid synthesis regulatory protein Opi1p by protein kinase A. *J. Biol. Chem.* 278:20673–20680. https://doi.org/10.1074/jbc.M300132200

Stace, C.L., and N.T. Ktistakis. 2006. Phosphatidic acid- and phosphatidylserine-binding proteins. *Biochim. Biophys. Acta.* 1761:913–926. https://doi.org/10.1016/j.bbalip.2006.03.006

Surma, M.A., C. Klose, D. Peng, M. Shales, C. Mrejen, A. Stefanko, H. Braberg, D.E. Gordon, D. Vorkel, C.S. Ejsing, et al. 2013. A lipid E-MAP identifies Ubx2 as a critical regulator of lipid saturation and lipid bilayer stress. *Mol. Cell.* 51:519–530. https://doi.org/10.1016/j.molcel.2013.06.014

Testerink, C., and T. Munnik. 2011. Molecular, cellular, and physiological responses to phosphatidic acid formation in plants. *J. Exp. Bot.* 62:2349–2361. https://doi.org/10.1093/jxb/err079

van der Walt, S., S.C. Colbert, and G. Varoquaux. 2011. The NumPy array: A structure for efficient numerical computation. *Comput. Sci. Eng.* 13:22–30. https://doi.org/10.1109/MCSE.2011.37

Vanommeslaeghe, K., E. Hatcher, C. Acharya, S. Kundu, S. Zhong, J. Shim, E. Darian, O. Guvench, P. Lopes, I. Vorobyov, and A.D. Mackerell Jr. 2010. CHARMM general force field: A force field for drug-like molecules compatible with the CHARMM all-atom additive biological force fields. *J. Comput. Chem.* 31:671–690. https://doi.org/10.1002/jcc.21367

Velázquez, A.P., T. Tatsuta, R. Ghillebert, I. Drescher, and M. Graef. 2016. Lipid droplet-mediated ER homeostasis regulates autophagy and cell survival during starvation. *J. Cell Biol.* 212:621–631. https://doi.org/10.1083/jcb.201508102

Walter, P., and D. Ron. 2011. The unfolded protein response: from stress pathway to homeostatic regulation. *Science.* 334:1081–1086. https://doi.org/10.1126/science.1209038

Wang, X., S.P. Devaiah, W. Zhang, and R. Welti. 2006. Signaling functions of phosphatidic acid. *Prog. Lipid Res.* 45:250–278. https://doi.org/10.1016/j.plipres.2006.01.005

Wassenaar, T.A., K. Pluhackova, R.A. Böckmann, S.J. Marrink, and D.P. Tieleman. 2014. Going backward: A flexible geometric approach to reverse transformation from coarse grained to atomistic models. *J. Chem. Theory Comput.* 10:676–690. https://doi.org/10.1021/ct400617g

Wassenaar, T.A., H.I. Ingólfsson, R.A. Böckmann, D.P. Tieleman, and S.J. Marrink. 2015. Computational lipidomics with insane: A versatile tool for generating custom membranes for molecular simulations. *J. Chem. Theory Comput.* 11:2144–2155. https://doi.org/10.1021/acs.jctc.5b00209

White, M.J., J.P. Hirsch, and S.A. Henry. 1991. The OPI1 gene of Saccharomyces cerevisiae, a negative regulator of phospholipid biosynthesis, encodes a protein containing polyglutamine tracts and a leucine zipper. *J. Biol. Chem.* 266:863–872.

Wimley, W.C., and S.H. White. 1996. Experimentally determined hydrophobicity scale for proteins at membrane interfaces. *Nat. Struct. Biol.* 3:842–848. https://doi.org/10.1038/nsb1096-842

Wolinski, H., H.F. Hofbauer, K. Hellauer, A. Cristobal-Sarramian, D. Kolb, M. Radulovic, O.L. Knittelfelder, G.N. Rechberger, and S.D. Kohlwein. 2015. Seipin is involved in the regulation of phosphatidic acid metabolism at a subdomain of the nuclear envelope in yeast. *Biochim. Biophys. Acta.* 1851:1450–1464. https://doi.org/10.1016/j.bbalip.2015.08.003

Young, B.P., J.J.H. Shin, R. Orij, J.T. Chao, S.C. Li, X.L. Guan, A. Khong, E. Jan, M.R. Wenk, W.A. Prinz, et al. 2010. Phosphatidic acid is a pH biosensor that links membrane biogenesis to metabolism. *Science.* 329:1085–1088. https://doi.org/10.1126/science.1191026

Zhang, F., Z. Wang, M. Lu, Y. Yonekubo, X. Liang, Y. Zhang, P. Wu, Y. Zhou, S. Grinstein, J.F. Hancock, and G. Du. 2014. Temporal production of the signaling lipid phosphatidic acid by phospholipase D2 determines the output of extracellular signal-regulated kinase signaling in cancer cells. *Mol. Cell. Biol.* 34:84–95. https://doi.org/10.1128/MCB.00987-13

Zinser, E., C.D.M. Sperka-Gottlieb, E.V. Fasch, S.D. Kohlwein, F. Paltauf, and G. Daum. 1991. Phospholipid synthesis and lipid composition of subcellular membranes in the unicellular eukaryote Saccharomyces cerevisiae. *J. Bacteriol.* 173:2026–2034. https://doi.org/10.1128/jb.173.6.2026-2034.1991